JGR Space Physics

RESEARCH ARTICLE
10.1029/2021JA029820

Key Points:

- High-frequency whistler waves at the bow shock behind the terminator and foreshock transients are investigated
- Resonant electron interaction with whistler waves is analyzed quantitatively
- Nonlinear resonant phase trapping by whistler waves is shown to cause effective electron acceleration

Correspondence to:
A. V. Artemyev,
aartemyev@igpp.ucla.edu

Citation:
Artemyev, A. V., Shi, X., Liu, T. Z., Zhang, X.-J., Vasko, I., Angelopoulos, V., & (2022). Electron resonant interaction with whistler waves around foreshock transients and the bow shock behind the terminator. *Journal of Geophysical Research: Space Physics*, *127*, e2021JA029820. https://doi.org/10.1029/2021JA029820

Received 21 JUL 2021
Accepted 24 JAN 2022

Electron Resonant Interaction With Whistler Waves Around Foreshock Transients and the Bow Shock Behind the Terminator

A. V. Artemyev[1,2], X. Shi[1], T. Z. Liu[1,3,4], X.-J. Zhang[1], I. Vasko[2,5], and V. Angelopoulos[1]

[1]Department of Earth, Planetary, and Space Sciences, University of CA, Los Angeles, CA, USA, [2]Space Research Institute of Russian Academy of Sciences, Moscow, Russia, [3]Cooperative Programs for the Advancement of Earth System Science, University Corporation for Atmospheric Research, Boulder, CO, USA, [4]Geophysical Institute, University of Alaska Fairbanks, Fairbanks, AK, USA, [5]Space Sciences Laboratory, University of California at Berkeley, Berkeley, CA, USA

Abstract Investigation of electron energization at (and around) the Earth's bow shock is critical to our understanding of space weather and astrophysical phenomena. The traditional adiabatic mechanisms for such energization compete with transient wave-particle interactions there. One of the most intense wave modes resonating with electrons is the high-frequency whistler mode, which is widely observed at (and around) the Earth's bow shock. Here, we examine these interactions in the context of the strong magnetic field gradients often found near the bow shock and at foreshock transients. Using THEMIS and ARTEMIS wave measurements, we quantify the nonlinear effects of resonant interactions between ≥100 eV electrons and intense coherent whistler waves. Such nonlinear interactions include the electron phase trapping by waves. As a result, the trapped electrons gain an energy up to several hundreds of eV. We estimate the main characteristics of the proposed acceleration mechanism and discuss its applicability to realistic plasma and magnetic field distributions.

1. Introduction

Electromagnetic whistler waves, with frequencies between lower-hybrid frequencies and electron cyclotron frequencies, are commonly observed in planetary magnetospheres and in the solar wind. These waves are driven by various types of electron anisotropy: thermal anisotropy (e.g., C. Kennel, 1966; Sagdeev & Shafranov, 1961), flow anisotropy (e.g., Sauer et al., 2020), or heat flux (Gary & Feldman, 1977; Tong et al., 2019; Vasko et al., 2020). This type of waves plays an important role in electron scattering and heating that are commonly described within the quasi-linear approximation (C. F. Kennel & Engelmann, 1966; Trakhtengerts, 1966; Vedenov et al., 1962). Conditions that favor whistler wave generation (e.g., dominant electron transverse anisotropy) are typically observed in the presence of adiabatic betatron heating (due to plasma compression) and/or loss cone anisotropy. The most thoroughly investigated whistler waves in the Earth's inner magnetosphere (see, e.g., reviews by Agapitov et al., 2018; Artemyev, Agapitov et al., 2016; Li & Hudson, 2019; Ni et al., 2016; Sazhin, 1993) are generated by electrons transversely heated during nightside plasma injections (Le Contel et al., 2009; Tao et al., 2011; X. Zhang, Thorne, et al., 2018) and dayside magnetic field compressions (Li et al., 2015). A similar mechanism of electron adiabatic heating and whistler wave generation (enhanced by large electron loss cone anisotropy) operates in the Earth's bow shock (Tokar et al., 1984; Veltri & Zimbardo, 1993a) and around foreshock transients (Shi et al., 2020).

The important role of whistler waves in Earth's inner magnetosphere (Horne, 2007; Thorne et al., 2010, 2013) has spurred extensive investigations on wave-particle resonant interaction that are not limited by the quasi-linear diffusion. One of the most interesting resonant interaction regimes is the nonlinear regime (Karpman et al., 1974; Nunn, 1971), which includes effects such as phase trapping and phase bunching (see reviews by Omura et al., 1991; Shklyar & Matsumoto, 2009; Albert et al., 2013; Artemyev et al., 2018, and references therein). This regime encompasses nondiffusive electron acceleration by coherent, intense whistler-mode waves propagating in an inhomogeneous magnetic field (e.g., Artemyev et al., 2012; Bell, 1984; Demekhov et al., 2006; Omura et al., 2007; Solovev & Shkliar, 1986). Well investigated and validated (Agapitov et al., 2015; Foster et al., 2014; Gan et al., 2020) in the Earth's inner magnetosphere, this regime has not been investigated for whistlers in the Earth's bow shock (although Y. Zhang et al., 1999 discussed the possible importance of such a regime for the shaping of electron distributions in the bow shock). In the next section, we will briefly review whistler-mode

waves around the bow shock to demonstrate that the nonlinear regime of wave-particle interaction is likely operating there and needs to be examined.

One of the first analyses of whistler waves in the Earth's bow shock demonstrated that locally measured electron distributions are fairly unstable to quasi-parallel waves with the primary source region around the shock foot (Greenstadt et al., 1981; Tokar et al., 1984). Although waves can scatter and isotropize electron distributions in the quasi-linear diffusion regime (Veltri & Zimbardo, 1993b), their high amplitudes ($\leq$1 nT) and coherent propagation highlight the potential importance of nonlinear wave-particle interactions (Y. Zhang et al., 1999). Using polar and wind spacecraft observations in the Earth's bow shock, Hull et al. (2012) and Wilson et al. (2013) demonstrated large-amplitude, field-aligned whistler waves with wave packets consisting of $\sim$10 cycles (wave periods) (Note this is also the typical wave-packet size for intense whistler-mode waves in the inner magnetosphere; X. J. Zhang, Thorne, et al., 2018). Although more recent observations from the MMS spacecraft showed additional direct evidence of resonant interaction between whistler-mode waves and suprathermal electrons in the Earth's bow shock (Oka et al., 2017), details of the electron acceleration mechanism have not yet been clarified. Oka et al. (2019) suggested that whistler waves are sufficiently intense to scatter electrons in a nonresonant regime, whereas Amano et al. (2020) suggested that electron acceleration is provided by a combination of whistler scattering and classical shock drift acceleration (Burgess, 1987; Decker, 1988; Decker & Vlahos, 1985). Both acceleration mechanisms (nonresonant scattering and combined scattering and shock-drift acceleration) assume multiple wave-particle interactions and thus resemble the quasi-linear mechanism. Observed whistler-mode waves are intense and coherent, however (Hull et al., 2012; Oka et al., 2019; Page et al., 2021; Wilson et al., 2013), which suggests that the nonlinear regime of resonant interaction could be also important.

Resonant electron interaction with whistler waves has long been thought to be effective in electron pitch-angle scattering (Bell & Inan, 1981; C. F. Kennel, 1969; Lyons et al., 1972; Shklyar, 1981). Therefore, at Earth's bow shock this interaction has been studied mostly to explain electron isotropization (Veltri & Zimbardo, 1993b). On microscales, such electron isotropization can support additional heating by the shock electric field and cross-shock electrostatic fields (Amano et al., 2020; Gedalin, 2020; Oka et al., 2017; T. Z. Liu et al., 2019). Moreover, acting with magnetic pumping by compressional low-frequency waves, pitch-angle scattering by whistler waves can generate suprathermal electron populations (Lichko & Egedal, 2020; Oka et al., 2019). Intense whistler waves, however, can do more than just pitch-angle scattering: they can also accelerate electrons via phase trapping in a strongly inhomogeneous magnetic field. This effect is well known in the Earth's inner magnetosphere (Albert et al., 2013; Shklyar & Matsumoto, 2009) and may be important for electrons around the bow shock. Kuramitsu and Krasnoselskikh (2005a) demonstrated that such trapping is possible for electrons moving across the strong electrostatic field in the bow shock. Trapping of bow shock electrons by an electrostatic field has also been shown in Ucer and Shapiro (2001). But nonlinear effects of trapping in the presence of strong magnetic field gradients and intense whistler waves have not yet been systematically quantified.

We examine electron resonant interaction with whistler waves observed in two systems (a) dayside foreshock transients (Z. Liu et al., 2015; Turner et al., 2013) and (b) Earth's bow shock behind the terminator. We focus on these systems rather than the dayside bow shock mostly for theoretical purposes. Ion and electron distributions are extremely unstable at typically supercritical dayside bow shock (e.g., Gedalin, 1999; Muschietti & Lembège 2017), where a wide range of waves and electromagnetic dynamical phenomena (Krasnoselskikh et al., 2013; Wilson, 2016) commonly exist. Thus, it is easier to isolate and investigate effects of whistler waves on electrons in less dynamical systems, such as a weak bow shock behind the terminator and foreshock transients.

We start by describing spacecraft observations in Section 2, where the main wave characteristics for two events in foreshock transients and two events in the weak bow shock behind the terminator are shown. We then present basic equations of electron resonant interaction with whistler waves (see Section 3.1) and effects of phase trapping (see Section 3.2). In Section 3.3, we model electron acceleration using observed background and wave characteristics. A discussion of our results and conclusions are given in Section 4.

2. Spacecraft Observations

We use THEMIS (Angelopoulos, 2008) and ARTEMIS (Angelopoulos, 2011) observations in the dayside foreshock and at the weak bow shock behind the terminator (around lunar orbit). Foreshock transients and bow shock crossings were identified using measurements from fluxgate magnetometers (with 1/5 s resolution; see Auster

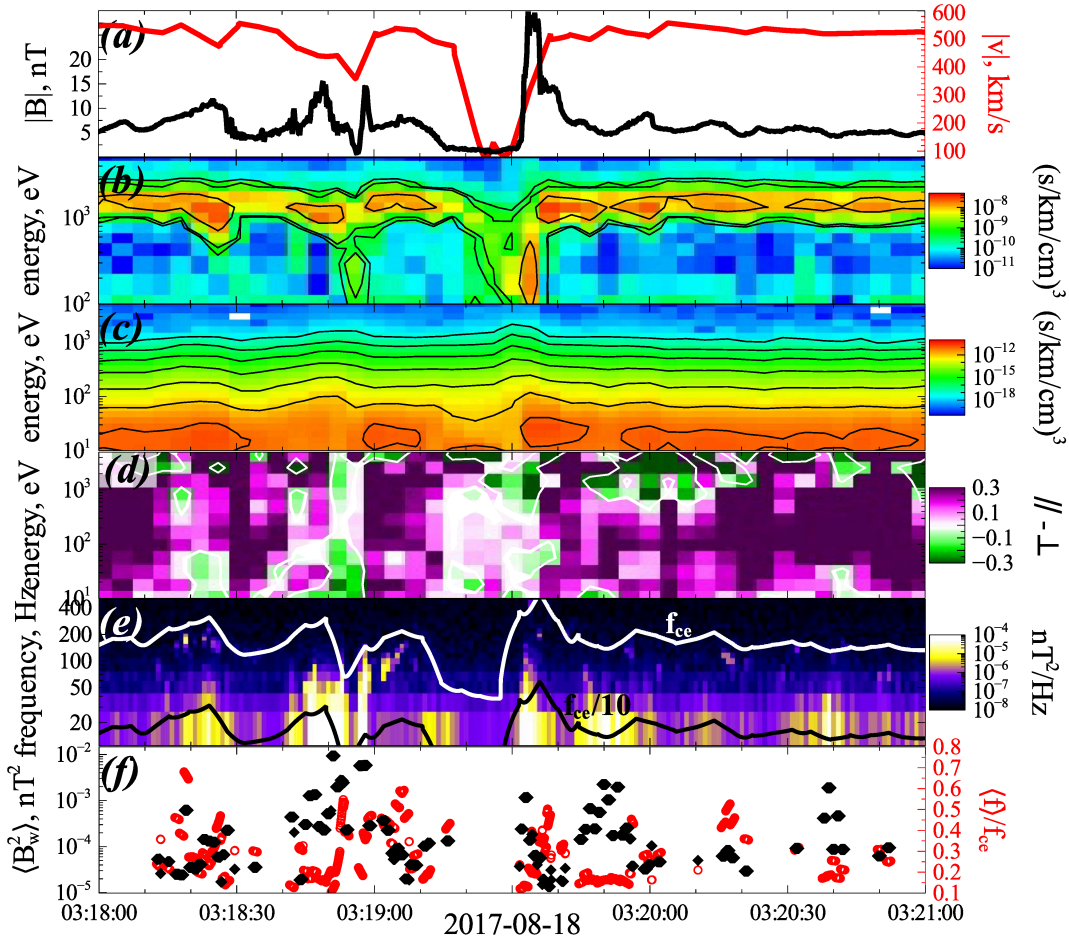

Figure 1. Overview of event #1: foreshock transient captured by THEMIS-E. (a) Magnetic field intensity and solar wind plasma flow in the GSE coordinates; omnidirectional (b) ion and (c) electron energy spectra; (d) electron flux anisotropy, $(f_\parallel - f_\perp)/(f_\parallel + f_\perp)$ with $f_\parallel, f_\perp$ being averaged fluxes over pitch angles $\in$ [0, 30]°, [150, 180]° and $\in$ [75, 105]°; (e) whistler wave frequency spectrum $\mathcal{B}_w^2$ with horizontal curves showing local f_{ce} and $f_{ce}/10$; (f) whistler-mode wave intensity $B_w^2 = \int_{f_{ce}/10}^{f_{ce}} \mathcal{B}_w^2 df$ and mean frequency $\int_{f_{ce}/10}^{f_{ce}} f \mathcal{B}_w^2 df / \int_{f_{ce}/10}^{f_{ce}} \mathcal{B}_w^2 df$.

et al., 2008) and ion and electron electrostatic analyzers that provide <25 keV spectra and moments with 3 − 4s resolution (McFadden et al., 2008). Whistler waves were analyzed based on measurements from search-coil (Le Contel et al., 2008) and electric field probes (Bonnell et al., 2008). We used both waveforms available during burst mode and wave spectra (FFF data set), which are routinely available during fast survey with 1 s resolution (Cully et al., 2008). We start by analyzing two foreshock transient events then two bow shock crossing events behind the terminator.

2.1. Foreshock Transients

Figures 1 and 2 show an overview of two events in foreshock transients, that is, foreshock bubbles within which reflected ions interact with the solar wind discontinuity and result in localized plasma compression and heating at the leading edge of the bubble (Omidi et al., 2010; Turner et al., 2013; A detailed description of the basic properties of and selection criteria for these transients, foreshock bubbles, can be found in T. Z. Liu et al., 2016). Panels (a) and (b) show magnetic field enhancement and decrease of plasma flow speed (caused by ion reflection) around 03:19:32 UT and 22:45:50 UT, which characterize the foreshock transients under consideration. Around transients, electron phase space density shows an increase in the suprathermal population with energies >100 eV (see panel (c)). This heated electron population is transversely anisotropic (see panel d). Enhanced suprathermal electron fluxes are associated with intense whistler waves observed within the $f/f_{ce} \in [0.1, 0.5]$ frequency range (see panel e). The average whistler-mode wave amplitude reaches ~100 pT (panel f), that is, ~0.1% of the

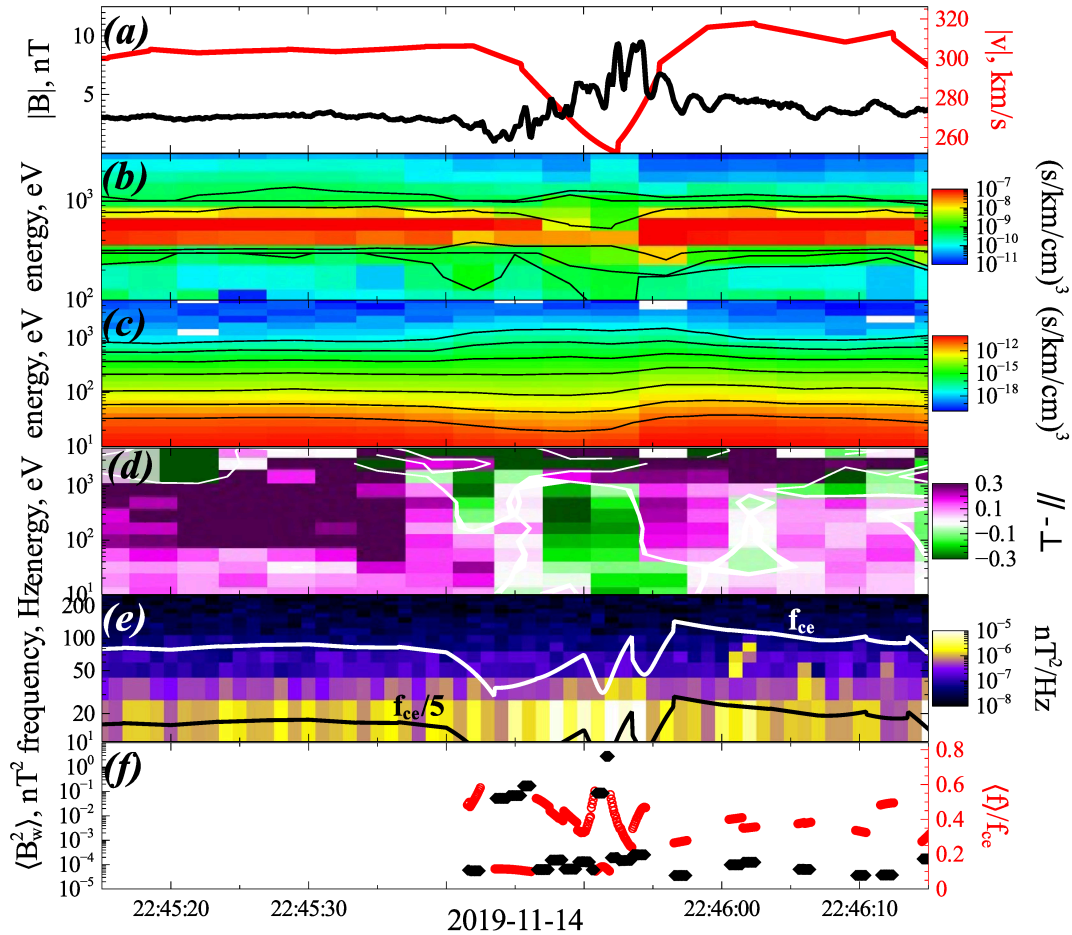

Figure 2. Overview of event #2: foreshock transient captured by THEMIS-D, in the same format as Figure 1.

background magnetic field, whereas examples of wave packets (in waveforms) show peak amplitudes of ∼1 nT. These highly intense whistler waves can actually resonate with electrons nonlinearly (similarly to observations in the inner magnetosphere, e.g., X. J. Zhang et al., 2019).

Foreshock transients (and associated whistler waves) in Figures 1 and 2 are very typical (see statistical results in Z. Liu et al., 2015; Shi et al., 2020; Turner et al., 2013). These local magnetic field enhancements compress plasma and can drive adiabatic electron heating (T. Z. Liu et al., 2019). Because they are magnetized, electrons are heated anisotropically, and thus their distribution becomes unstable. Relaxation of this instability leads to whistler wave generation. Note that the observed whistler waves are well localized around magnetic field enhancements. These waves can interact with ambient electrons near magnetic field gradients. Around the magnetic field gradient, electron pitch angles can vary significantly due to the mirror force. With these pitch-angle variations (i.e., variations of the electron parallel velocity), even electrons that are initially nonresonant can fall into resonance with whistler waves. Using electron spectra and whistler wave characteristics in Section 3.3, we model such resonant interaction.

2.2. Bow Shock Behind the Terminator

Figures 3 and 4 show two examples of ARTEMIS P1 crossings of the bow shock behind the terminator. During these two events, quasi-perpendicular shocks with a well-defined ramp (see panel a) were encountered. Ion and electron heating across the shock (see panel b and c) is accompanied by formation of an anisotropic electron population with energies ∈ [0.1, five] keV (see panel d). Immediately behind the shock ramp, in the downstream, ARTEMIS observed intense whistler waves with frequencies $f \in [0.1, 0, 5]f_{ce}$ (see panel e and f). Thus, it is likely that the electron compressional heating at the shock leads to the transversely anisotropic electron population

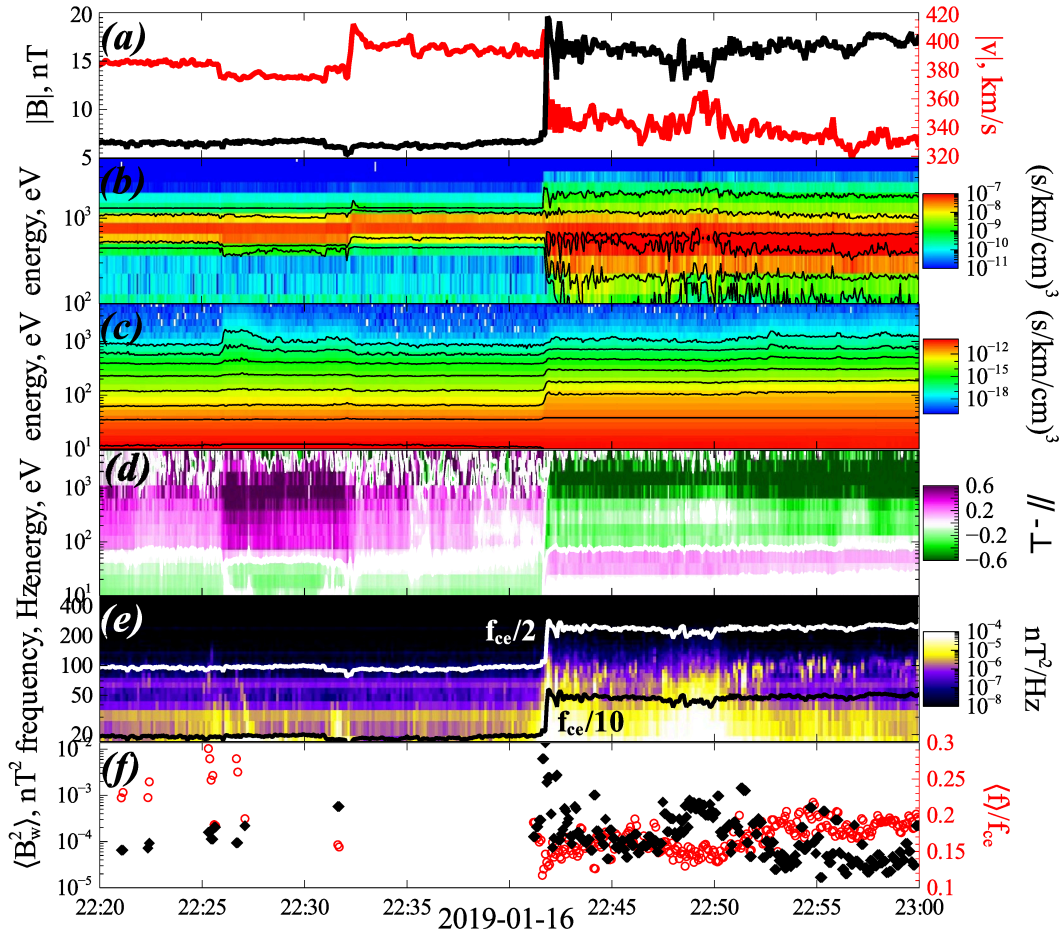

Figure 3. Overview of event #3, which was captured by ARTEMIS P1. (a) Magnetic field intensity and solar wind plasma flow in GSE coordinates; omnidirectional (b) ion and (c) electron energy spectra; (d) electron flux anisotropy $(f_{\parallel} - f_{\perp})/(f_{\parallel} + f_{\perp})$, with $f_{\parallel}, f_{\perp}$ being the average fluxes with pitch angles $\in$ [0, 30]°, [150, 180]° and $\in$ [75, 105]°; (e) whistler-mode wave frequency spectrum with horizontal curves showing local f_{ce} and $f_{ce}/10$; (f) whistler-mode wave intensity and mean frequency.

and further energy release via whistler wave generation. Although the average wave amplitude reaches ~100 pT (see panel f), wave packets show peak amplitudes up to 1 nT, in agreement with previous findings about intense whistler-mode waves at the dayside bow shock (Hull et al., 2012; Wilson et al., 2013). Typical wave packets have ~10 wave periods (see Figure 5).

Figures 3 and 4 show electron compressional heating, anisotropy formation, and whistler wave bursts, similar to those shown in foreshock transients (compare with Figures 1 and 2). Thus, we will adopt the same approach to investigate whistler-mode wave interaction with electrons in both systems.

3. Electron Resonant Interaction With Whistler Waves

In this section, we discuss the main effects of electron resonant interaction with whistler waves in the presence of strong magnetic field gradients. We focus on nonlinear resonant interaction and mostly analyze test particle results and theoretical interpretations of these results (for detailed, stricter analytical approaches see, e.g., Albert, 1993; Artemyev et al., 2018; Shklyar & Matsumoto, 2009).

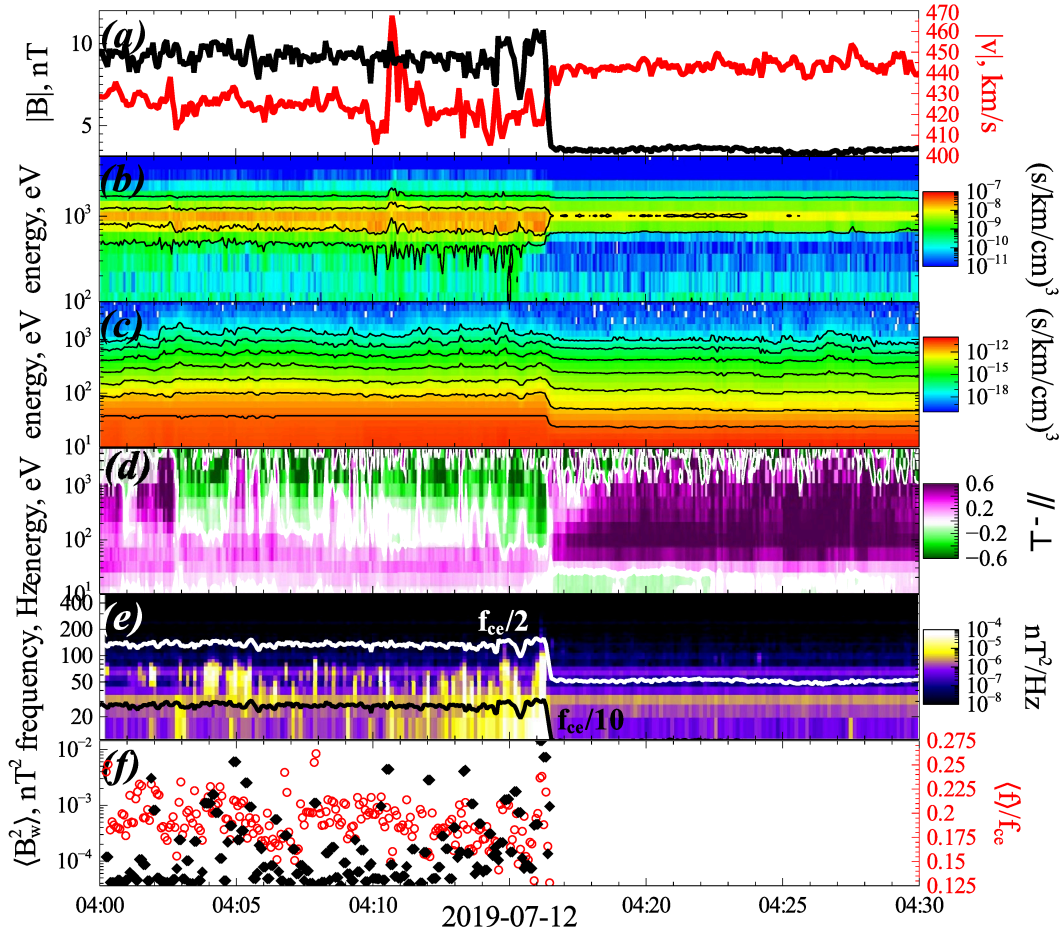

Figure 4. Overview of event #4, which was captured by ARTEMIS P1, in the same format as Figure 3.

3.1. Basic Equations

Let us start with the system with a magnetic field gradient to examine nonrelativistic electron (mass m_e, charge $-e$) dynamics around this gradient. Although the gradient direction can be mostly transverse to the background magnetic field direction, the magnetized electron motion is mostly along magnetic field lines. Thus, even a small magnetic field component along the magnetic field gradient will reduce equations of motion to 1D gyroaveraged equations with the Hamiltonian (Leroy & Mangeney, 1984; Wu, 1984):

$$H = \frac{1}{2m_e}p_\parallel^2 + \mu B\left(s + v_D t\right) - e\varphi\left(s + v_D t\right) \tag{1}$$

where $(s, p_\parallel)$ are conjugate field-aligned coordinate and momentum, v_D is the velocity of the magnetic field gradient in the electron reference frame, μ is the magnetic moment, and $\varphi(s)$ is the large-scale electrostatic potential caused by decoupling of ion and electron motions around the magnetic field gradient (Goodrich & Scudder, 1984; Scudder, 1995). Note that estimate of v_D requires analysis of the shock configuration, but for our analysis of wave-particle resonant interaction, v_D magnitude is not important (To illustrate the role of v_D, we examined results with $v_D \in [500, 5000]$km/s that corresponds to a wide range of the shock normal angle; see, e.g., Wu, 1984 for v_D equation).

Field-aligned whistler waves can be included in a Hamiltonian (1) as (e.g., Karpman, 1974)

$$H = \frac{1}{2m_e}p_\parallel^2 + \mu B\left(\tilde{s}\right) - e\varphi\left(\tilde{s}\right) + \sqrt{\frac{\mu B\left(\tilde{s}\right)}{m_e}}\frac{eB_w}{ck} f(\phi)\sin\left(\phi - \theta\right), \quad \phi = \int^{s} k\left(s'\right) ds' - \omega t \tag{2}$$

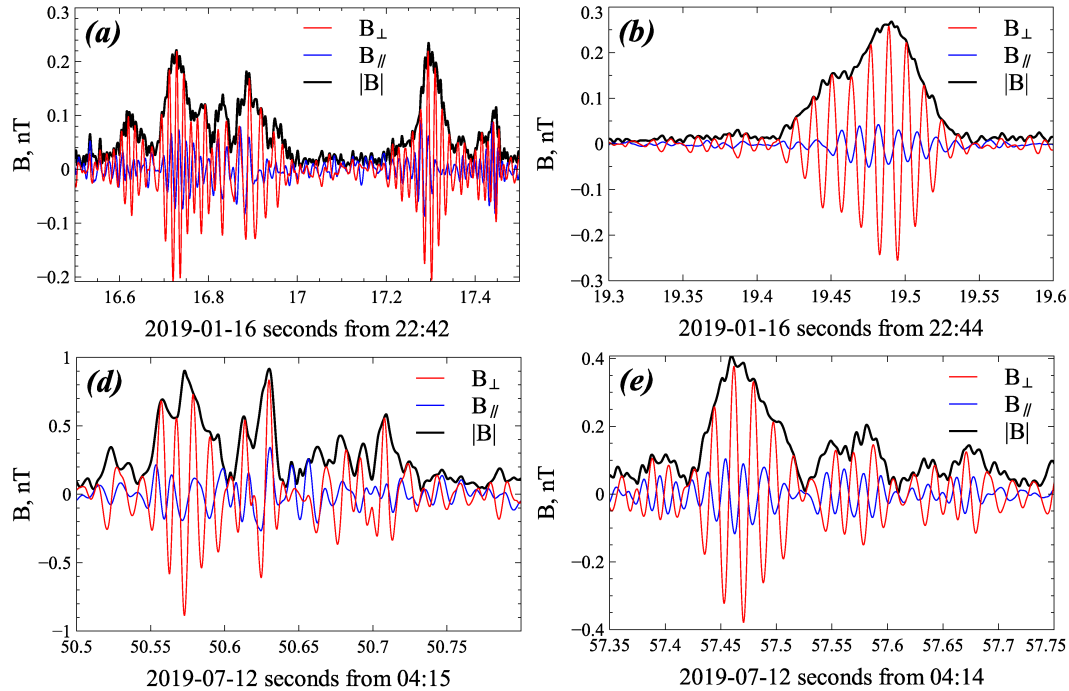

Figure 5. Sample whistler wave packets for events in (a–b) Figure 3 and (c–d) Figure 4.

where the wave amplitude B_w (in realistic wave models B_w can be set as a function of $\tilde{s} = s + v_D t$), the electron gyrophase is given by $\dot{\theta} = -eB(s)/m_e c$, and the wavevector is determined from the cold plasma dispersion relation (Stix, 1962) and also depends on $\tilde{s}$ (further we use s rather than $\tilde{s}$).

Specifically, the following magnetic field, plasma, or wave distributions were adopted for the wave model in Hamiltonian (2):

1. To mimic the background magnetic field topology, we use a simplified magnetic field model with a prescribed gradient $B(s) = B_0 + (B_\infty - B_0) \cdot (1 + \tanh(s/L))/2$, where the spatial scale L is much larger than the whistler wave wavelength ($kL \gg 1$). Parameters B_0 and B_∞ determine magnetic field intensity ahead of the gradient (upstream of the shock) and behind the gradient (downstream of the shock)
2. The cold plasma density $n(s)$ is assumed to follow the magnetic field profile $n(s) \sim B(s)$, and thus the ratio of plasma to gyrofrequencies (important for the whistler wave dispersion relation) equals to $\omega_{pe}\sqrt{B_\infty/B(s)}$, where $\omega_{pe} = \text{const}$ and $\omega_{pe} m_e c/eB_\infty$ is one of the main model parameter. We determine ω_{pe} from spacecraft observations behind the magnetic field gradient (e.g., downstream of the shock)
3. Large-scale electrostatic potential φ is very important in heating solar wind electrons, and its magnitude varies from a few tens of eV (Mozer & Sundkvist, 2013; Schwartz et al., 2011) to a few hundreds of eV (Dimmock et al., 2012; Lefebvre et al., 2007; Schwartz et al., 2021; Walker et al., 2004). Thus, to examine the role of this potential on the electron resonant interaction with whistler waves, we assume $\varphi = \varphi_0 \cdot \tanh(s/L)$ (e.g., Gedalin, 1996; Gedalin, 2020)
4. To mimic the whistler wave propagation in the form of wave packets (as in the observations), we use $f(\phi)$ to describe the wave packet size. For $f = 1$, we deal with a plane wave, and if $f(\phi)$ is a localized function ($f \to 0$ for $|\phi| \gg \delta\phi$), we deal with a wave packet of the size of $2\delta\phi$. Wave packet size is measured in wave lengths, and we assume $f(\phi) = \exp\left(-(\phi/40\pi)^2\right)$, which describes the wave packet with the size of ~20 wave lengths. For $|\phi/2\pi| > 10$, the wave intensity exponentially decays
5. To model wave distributions around the magnetic field gradient, we assume B_w as $B_w = B_{w0}\exp(-s^2/R^2)$, where B_{w0} is the peak amplitude, R is the typical spatial scale of the whistler wave. This function guarantees that waves would not propagate too far from their generation region
6. As wave frequency ω is determined by the generation conditions on (or behind) the magnetic field gradient (i.e., at strong background magnetic field), we should restrict whistler waves to a region that $eB(s)/m_e c$ remains larger than ω (i.e., ω should not exceed the local electron gyrofrequency). For this reason, we modify

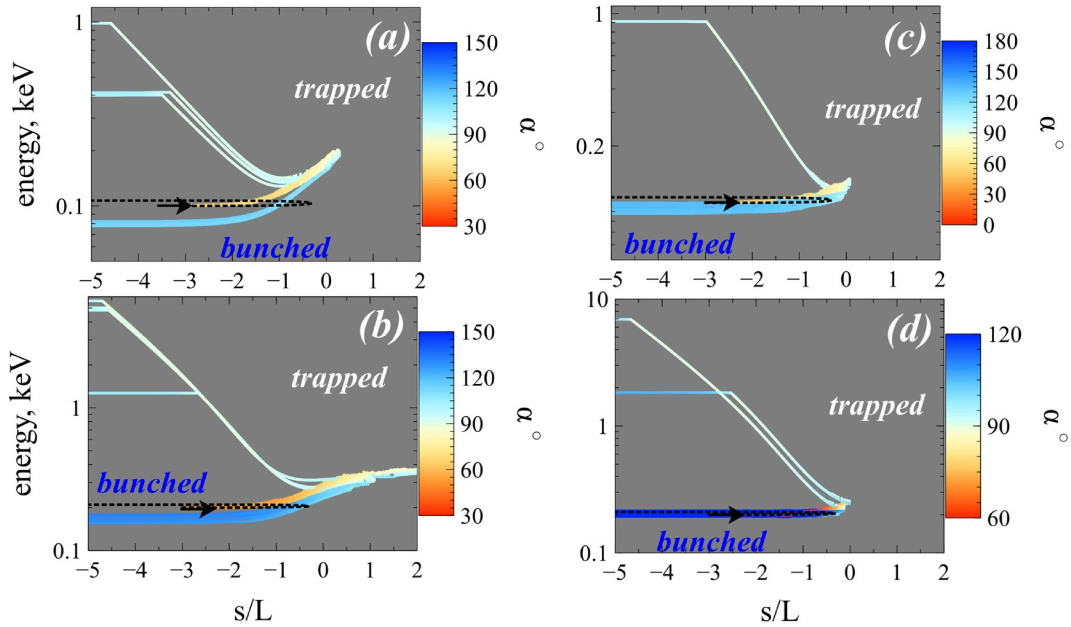

Figure 6. Test particle trajectories of electrons with different initial energies for $B_\infty/B_0 = 3$. Each panel includes 10 trajectories; arrows indicate the initial direction of electron motion and color shows the instantaneous electron pitch angle. Initial electron pitch angle and energy are: (a) 65° and 100 eV; (b) 50° and 200 eV; (c) 50° and 100 eV; (d) 50° and 200 eV. The electrostatic potential magnitude is $\varphi_0 = 200$ eV for (a) and (b) and $\varphi_0 = 50$ eV for (c) and (d), whereas $v_D = 500$ km/s.

B_w model to $B_w = B_{w0}\ \exp(-s^2/R^2) \cdot g(s)$, with $g(s) = \left(B(s) - \tilde{B}\right)/\left(B_\infty - \tilde{B}\right)$ and $\tilde{B} = m_e c\omega/e$. Function $g(s)$ equals to one at $B(s) = B_\infty$ (e.g., downstream of the shock) and equals to zero at $eB(s)/m_e c = \omega$

3.2. Phase Trapping and Phase Bunching

We start with characteristic electron trajectories described by a Hamiltonian (2) with system parameters typical of Earth's bow shock shown in Figures 3 and 4: $\omega_{pe} = 85eB_\infty/m_e c$, $B_\infty/B_0 = 3$, $L = 3000$ km, $B_{w0} = 250$ pT, $\omega m_e c/eB_\infty = 0.3$, $R = 5L$. Whistler waves propagate downstream (waves generated by electron thermal anisotropy have the same probability of propagating parallel or antiparallel to the magnetic field (Vasko et al., 2020), and we consider such waves that can resonate with electrons reflecting from the bow shock and moving from downstream to upstream; note that the electron resonant velocity from $\dot{\phi} - \dot{\theta} = 0$, $p_\parallel/m_e = (\omega - \Omega_{ce})/k$, is negative for whistler waves with $\omega < \Omega_{ce}$, that is, resonant electrons and waves should propagate in opposite directions). Figures 6–8 show sets of electron trajectories with different initial energies/pitch angles and different φ_0, v_D: for each set we show trajectories without whistler waves (dashed black curves) and trajectories with whistler waves (colored curves). Electrons with $\alpha < 90°$ move from downstream to upstream, whereas reflected electrons move back to upstream and have $\alpha > 90°$. All electron trajectories start at $s/L = -3$ and are integrated while $|s/L| < 5$.

We show sets of 10 trajectories for different energies and pitch angles corresponding to electron reflection from magnetic field gradients (black dotted curves in Figures 6–8 show electron orbits in the absence of whistler waves). Waves trap electrons into resonance (resulting in electron acceleration) or scatter electrons leading to an energy loss (this nonlinear scattering is called phase bunching). For large v_D (quasi-perpendicular shock), the electron energy gain due to reflection from the gradient can exceed the energy loss due to the phase bunching (see Figure 8 with $v_D = 5000$ km/s). Tests with zero v_D, however, demonstrate the energy decrease for bunched electrons (not shown). This energy loss can serve as a source for whistler-mode wave amplification (see Hsieh et al., 2020; Shklyar, 2011; Shklyar, 2017), that is, a large population of phase-bunched particles (bunching is much more probable than phase trapping, see, e.g., Artemyev, Neishtadt, et al., 2016; Shklyar, 2011; Vainchtein et al., 2018) provides energy to whistler waves that further transfer this energy to phase-trapped electrons (Omura et al., 2008; Solovev & Shkliar, 1986; Shklyar, 2011). And, indeed, acceleration of test electrons trapped by waves is rather effective and (in realistic systems with energy conservation) requires considerable energy input to waves: Figures 6 and 7 show that trapping results in energy increases from

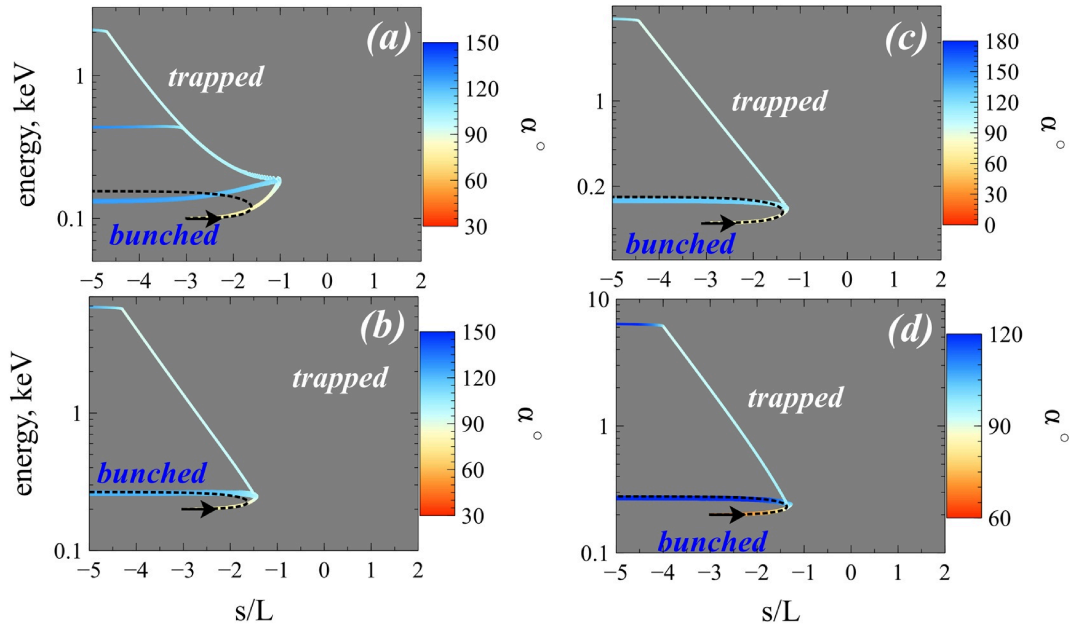

Figure 7. Test particle trajectories of electrons with different initial energies for $B_\infty/B_0 = 3$. Each panel includes 10 trajectories; arrows indicate the initial direction of electron motion and color shows the instantaneous electron pitch angle. Initial electron pitch angle and energy are: (a) 75° and 100 eV; (b) 75° and 200 eV; (c) 70° and 100 eV; (d) 70° and 200 eV. The electrostatic potential magnitude is $\varphi_0 = 200$ eV for (a) and (b) and $\varphi_0 = 50$ eV for (c) and (d), whereas $v_D = 1000$ km/s.

~100 eV to a few keVs. This acceleration mechanism resembles gyroresonant surfing acceleration (Kuramitsu & Krasnoselskikh, 2005a, 2005b) and shock surfing (e.g., Artemyev et al., 2014; Lever et al., 2001; Ucer & Shapiro, 2001). For trapped electrons, however, the wave force is balanced by the magnetic field gradient force $\mu dB/ds$ rather than electrostatic fields.

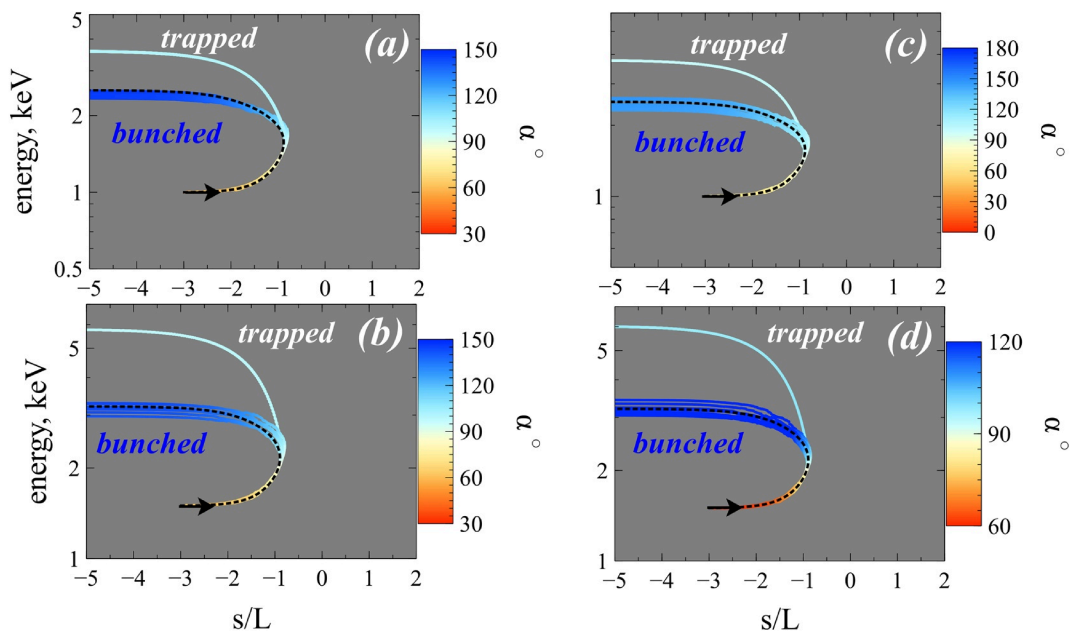

Figure 8. Test particle trajectories of electrons with different initial energies for $B_\infty/B_0 = 3$. Each panel includes 10 trajectories; arrows indicate the initial direction of electron motion and color shows the instantaneous electron pitch angle. Initial electron pitch angle and energy are: (a) 60° and 1 keV; (b) 60° and 1.5 eV; (c) 60° and 1 keV; (d) 60° and 1.5 eV. The electrostatic potential magnitude is $\varphi_0 = 200$ eV for (a) and (b) and $\varphi_0 = 50$ eV for (c) and (d), whereas $v_D = 5000$ km/s.

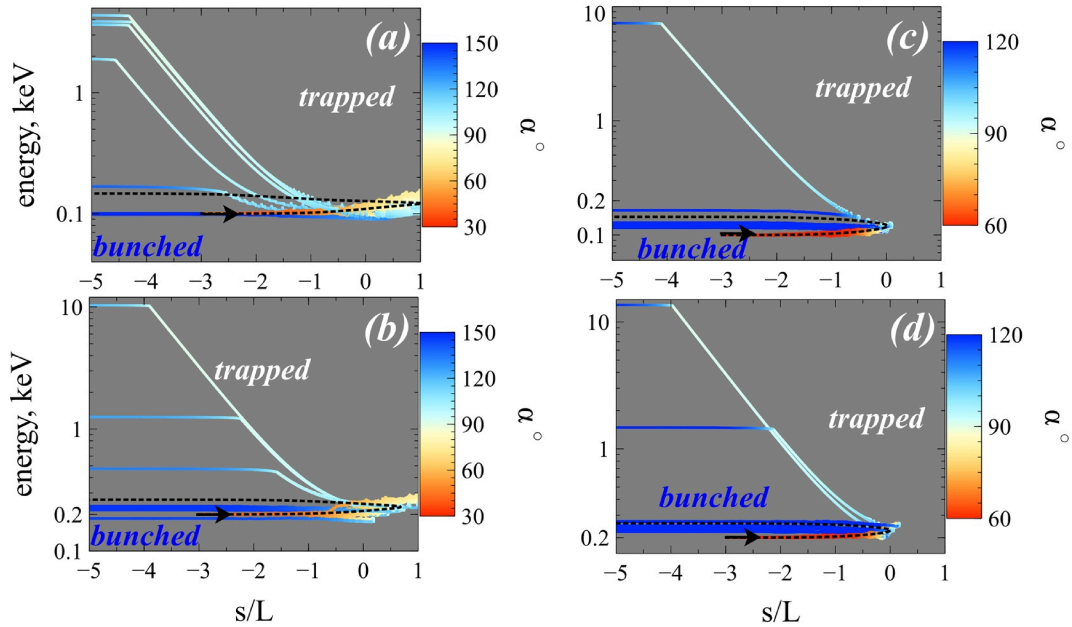

Figure 9. Test particle trajectories of different initial energies for $B_\infty/B_0 = 3$, $\varphi_0 = 0$, $v_D = 500$ km/s. Each panel includes 10 trajectories; arrows indicate the initial direction of electron motion and color shows the instantaneous electron pitch angle. Initial electron pitch angle and energy are: (a) 40° and 100 eV; (b) 40° and 200 eV; (c) 50° and 100 eV; (d) 50° and 200 eV.

For electron adiabatic motion (in the absence of wave-particle interaction), the electrostatic potential plays the same role as the potential energy and μB term, that is, electrons can cross the potential wall $U(s) = \mu B - e\varphi$ (if $p_\parallel^2/2m_e$ is large enough, i.e., if pitch angle is small enough) or can be reflected from this wall (if $p_\parallel^2/2m_e$ is small). The magnitude of the smaller potential determines the pitch-angle ranges of reflected and transient electrons (Leroy & Mangeney, 1984; Wu, 1984). Therefore, resonant whistler wave interactions with reflected electron can be similar for different φ magnitudes, but the pitch-angle range of resonant electrons is controlled by φ magnitude (compare panels a and b and c and d in Figure 6). Figures 9 and 10 confirm this idea and show resonant electron acceleration and scattering in the absence of electrostatic potential (compare Figures 6 and 9: for the same magnetic field configuration, resonant electrons have smaller initial pitch angles in the system with $\varphi = 0$). As φ does not change the energy of trapped (accelerated) electrons, for further analysis of electron acceleration by whistler-mode waves we assume $\varphi = 0$.

The resonant interaction with whistler-mode waves require rather small parallel velocities of electrons, and this determines that the interactions take place around electron mirror point (i.e., around electron reflection from the magnetic field gradient). Note in Figures 6–10 electron trapping acceleration leads to a pitch angle increase, and these accelerated electrons should thus form a transversely accelerated population. This pitch-angle increase from trapping occurs when almost all electron energy is perpendicular. Trapped electrons move with a negligibly small parallel velocity and their pitch angles remain at ~90°. Without phase trapping, electrons would be reflected from the magnetic field gradient and keep their high parallel velocity. The gradient front velocity v_D thus does not change the resonance, but controls what electron energies and pitch angles will be in the resonance. Comparison of Figures 6–8 shows that the same resonant trapping and acceleration is possible for a wide range of v_D, but for higher v_D the electron acceleration due to reflection from the magnetic field gradient can be more significant than electron energy lost due to the phase bunching. Therefore, both φ_0 and v_D are not so important for investigation of the electron resonant interactions with whistler-mode waves (and we fix $\varphi_0 = 0$, $v_D = 500$ km/s in following calculations), but should be evaluated and used for any investigations of the realistic shock waves and foreshock transients.

Electron energies shown in Figures 9 and 10 are higher than the solar wind electron temperature, and generally these electrons cannot resonate with whistler waves, because the resonant condition, $p_\parallel = (\omega m_e c - eB)/ck \sim m_e c\,(\Omega_{ce}/\omega_{pe})\sqrt{\Omega_{ce}/\omega} \sim m_e c/30$, cannot be satisfied for energies larger than a fraction of an electronvolt. However, the strong magnetic field gradient mirrors electrons by decreasing their parallel

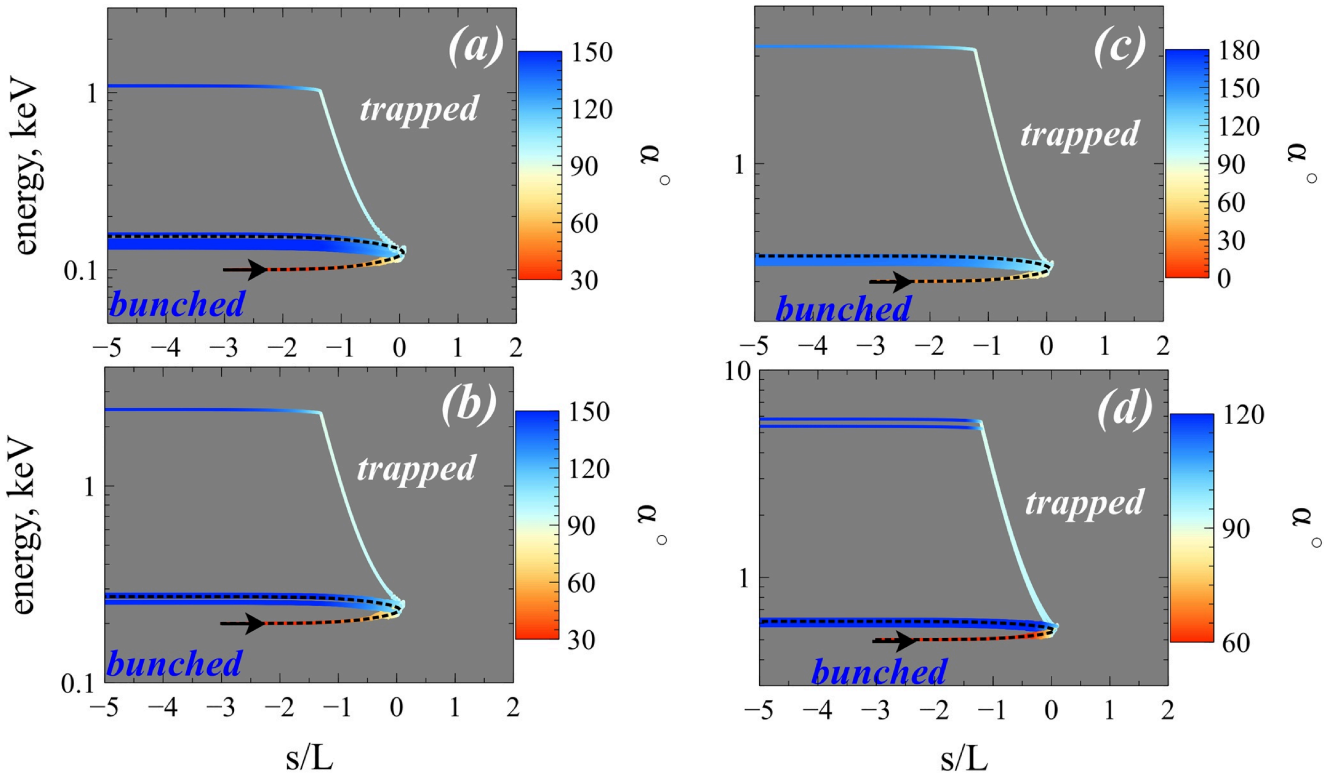

Figure 10. Test particle trajectories of different initial energies for $B_\infty/B_0 = 10$, $\varphi_0 = 0$, $v_D = 500$ km/s. Each panel includes 10 trajectories; arrows show the initial direction of electron motion and color shows the electron pitch angle. The initial electron pitch angle and energy are: 25° and 100 eV (a); 25° and 200 eV (b); 25° and 300 eV (c); 25° and 500 eV (d).

speed to almost zero, and even energetic particles can have very small $p_\parallel$ to resonate with whistler waves. The magnetic field jump B_∞/B_0 is higher for foreshock transients ($B_\infty/B_0 = 10$) than for the bow shock behind the terminator ($B_\infty/B_0 = 3$; see Figures 1–4). Thus, electron mirroring effects should be stronger for foreshock transients. Figure 10 shows results for $B_\infty/B_0 = 10$ and Figure 9 shows results for $B_\infty/B_0 = 3$. We see the same energy gain due to reflection from the moving magnetic field gradient for phase-bunched electrons with pitch angles increasing to $\alpha > 90°$ (i.e., electrons initially move toward the magnetic field increase, with $\alpha < 90°$, are reflected and move away with $\alpha > 90°$). Phase trapping efficiency is comparable for traces shown in Figures 9 and Fig. 10: trapped electrons (with an initial energy of 100–200 eV) can gain several keVs.

3.3. Energy Range of Accelerated Electrons

Figures 9 and 10 show that electron resonant interactions with whistler waves can result in effective phase trapping and acceleration. What are the typical energies gained by electrons in such a nonlinear acceleration regime? To estimate that energy gain, we use the invariant of the wave-particle resonant interaction with field-aligned whistler waves $p_\parallel^2 m_e/2 + \mu B - \mu\omega m_e c/e = const$ (Shklyar & Matsumoto, 2009) and the resonant condition $p_\parallel = (\omega - \Omega_{ce})/m_e k$ with $kd_e = (\Omega_{ce}/\omega - 1)^{-1/2}$ and $d_e = c/\omega_{pe}$. Combination of these equations gives

$$\frac{1}{2}\frac{m_e}{\omega}\Delta\left(d_e^2(\Omega_{ce}-\omega)^3\right) + \frac{m_e c}{e}\Delta\left(\mu\left(\Omega_{ce}-\omega\right)\right) = 0$$
$$\frac{1}{2}\frac{m_e}{\omega}\Delta\left(d_e^2(\Omega_{ce}-\omega)^3\right) + \frac{m_e c}{e}\Delta\left(\mu\Omega_{ce}\right) = \Delta H \quad (3)$$

where Δ represents the difference between the trapping position and the position of escape from the resonance. Equation 3 can be rewritten as

$$\Delta H = \frac{\frac{1}{2}m_e\Delta\left(d_e^2(\Omega_{ce}-\omega)^3\right)+\frac{m_e c}{e}\omega\mu^*\Delta\Omega_{ce}}{\omega-(\Omega_{ce}^*+\Delta\Omega_{ce})} \quad (4)$$

where star denotes values at the moment of trapping. Using a simple adiabatic relation between the plasma density and the magnetic field ($n \sim B$), d_e^2 can be rewritten as $d_e^2 = d_{e*}^2\Omega_{ce}^*/\Omega_{ce}$. Electron trapping occurs at $p_\parallel \sim 0$, that is, $\mu^*B^* \approx H_{\rm init}$. Thus, Equation 4 takes the form:

$$\begin{aligned}\frac{H_{final}}{H_{init}} &= \frac{\frac{1}{2}m_e d_{e*}^2\Delta\left(\frac{\Omega_{ce}^*}{\Omega_{ce}}(\Omega_{ce}-\omega)^3\right)+H_{init}\frac{\omega}{\Omega_{ce}^*}\Delta\Omega_{ce}}{\omega-(\Omega_{ce}^*+\Delta\Omega_{ce})}+1\\ &= 1+\frac{m_e c^2}{2H_{init}}\left(\frac{\Omega_{ce}^*}{\omega_{pe}^*}\right)^2\frac{\eta(1-\omega_m)^3-(\eta-\omega_m)^3}{\eta\,(\eta-\omega_m)}+\frac{(1-\eta)\,\omega_m}{\eta-\omega_m}\end{aligned} \quad (5)$$

where $\eta = 1+\Delta\Omega_{ce}/\Omega_{ce}^* < 1$ is the ratio of magnetic fields in the detrapping position to those in the trapping position, $\omega_m = \omega/\Omega_{ce}^*$. Typically $\omega_{pe}^*/\Omega_{ce}^* \sim 85$ and

$$\frac{H_{final}}{H_{init}} = 1+\frac{35\ \text{eV}}{H_{init}}\frac{\eta(1-\omega_m)^3-(\eta-\omega_m)^3}{\eta\,(\eta-\omega_m)}+\frac{(1-\eta)\,\omega_m}{\eta-\omega_m} \quad (6)$$

If whistler waves have low frequency with $\omega_{\rm m} \ll 1$, Equation 5 gives $H_{\rm final}/H_{\rm init} = 1 + (35\ {\rm eV}/H_{\rm init})\cdot(\eta^{-1}-\eta)$. For the bow shock with $\eta > 1/3$ we have $\Delta H < 100$ eV, whereas for foreshock transients with $\eta > 1/10$ we have $\Delta H < 350$ eV. If the whistler wave frequency $\omega_{\rm m}$ can approach η, however, the energy gain increases without limit (when a constant whistler wave magnitude is assumed; this assumption works until the wave is damped at around $\omega/\Omega_{\rm ce} \sim 1$).

3.4. Test Particle Results

To examine the effect of electron acceleration by whistler waves around magnetic field gradients, we use test particle simulations with wave characteristics from spacecraft observations. Separately for $B_\infty/B_0 = 3$ and $B_\infty/B_0 = 10$, we numerically integrate 10^7 electron trajectories with initially uniform energy distribution $\in$ [0.1, 10] keV and pitch-angle distribution $\in$ [0°, 90°] (this range corresponds to electrons moving from the solar wind toward the downstream region). For each trajectory, we randomly set wave amplitude $B_{\rm w} \in$ [0.1, 1]nT and wave frequency $\omega/\Omega_{\rm ce} \in$ [0.05, 0.5]. Thus, we produce a set of reflected electron trajectories with different energy gains, ΔE.

Figures 11a shows the distribution of 10^4 random trajectories in (ΔE, $E_{\rm init}$) space for the foreshock transient field model; colors denote the wave amplitude. We use the log-scale for ΔE, and thus do not show electrons with $\Delta E < 0$ (electrons that are decelerated due to phase bunching) in this panel. There are two particle populations. The population with $\Delta E < a\sqrt{E}$ corresponds to an energy change caused by reflection from the moving magnetic field gradient. This population does not depend on wave amplitude. The population with $\Delta E > a\sqrt{E}$, however, corresponds to an energy change caused by wave-particle interaction, and it occurs only with high wave amplitudes. Boundary $\Delta E = a\sqrt{E}$ can be obtained from the equations of the electron interaction with the motional magnetic field of the magnetic gradient. After being reflected from the magnetic field gradient, electrons move along the tangential electric field E_τ with an energy change $\dot{E} \approx eE_\tau\sqrt{2E/m_e}$, where $\sqrt{2E/m_e}$ is the typical electron speed. The reflection time is about an electron gyroperiod, $m_e c/eB_0$, and the energy change can be written as $\Delta E \approx m_e\left(\sqrt{2E_{init}/m_e}+2cE_\tau/B_0\right)^2/2 - E_{init} \approx 2cm_e\,(E_\tau/B)\sqrt{2E_{init}/m_e} \sim a\sqrt{E}$ for $\Delta E \ll E_{\rm init}$.

Using the distribution of $\Delta E(E_{\rm init}, B_{\rm w}, \omega)$ and the probability distribution of the observed solar wind energy spectrum and wave characteristics, we calculate the final energy spectrum of electrons interacting with magnetic field gradients. Figures 11b and 11c show examples of such spectra for events from Figures 1 and 2. The inset panels show probability distributions of observed waves in the ($B_{\rm w}$, $\omega/\Omega_{\rm ce}$) space. To rescale the $B_{\rm w}$ derived from the 1 s averaged spectrum to the actual wave-packet amplitude, we use a multiplication factor obtained by comparing actual wave form fields (see Figure 5) to 1 s averaged spectra. The spectra of electrons accelerated at the magnetic field gradient by waves show a [0.1, 1]keV increase in particles for both events. Some particles experience a >1 keV acceleration, however.

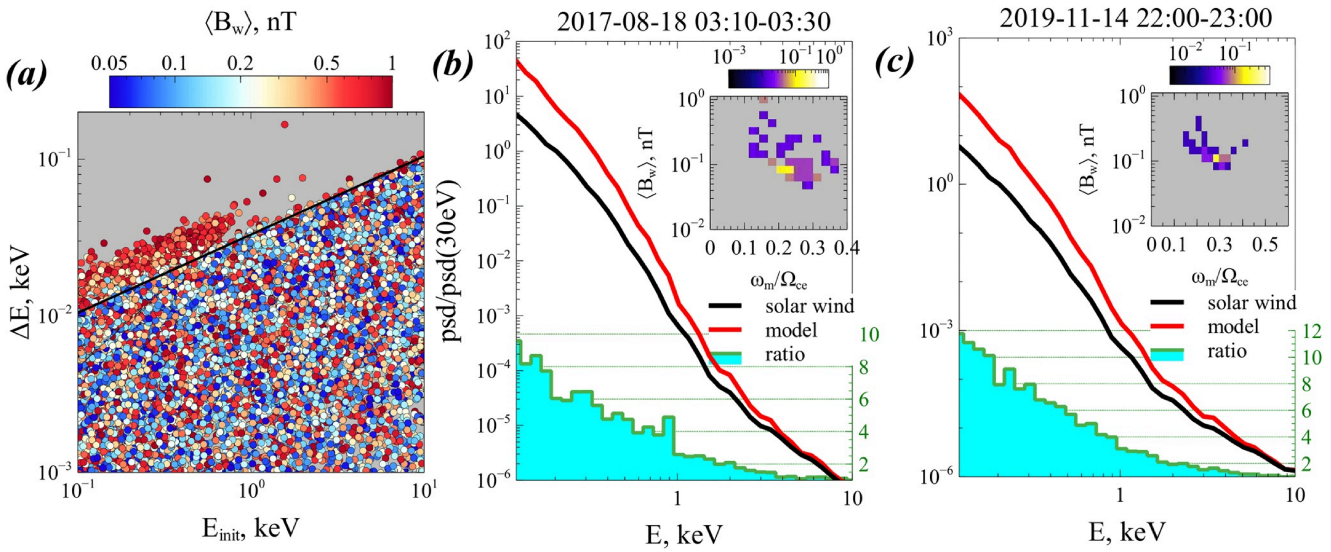

Figure 11. (a) Distribution of 10^4 particles randomly selected from 10^7 test particles in energy, energy gain space. Colors denote wave amplitudes used for each particle orbit. (b and c) Energy spectra of solar wind particles ahead of the foreshock transient (black) and particles accelerated by waves (red) and reflected by magnetic field gradient for events shown in Figures 1 and 2. The ratio of two spectra is shown to the right vertical axis. Inset panels show probability distributions of observed wave characteristics.

Using the same approach, we integrate 10^7 trajectories for $B_\infty/B_0 = 3$ (the bow shock configuration behind the terminator) and different wave amplitudes and frequencies. Figure 12a shows the distribution of 10^4 trajectories having $\Delta E > 0$ in $\Delta E(E_{init}, B_w, \omega_m)$ space with a clearly wave-accelerated electron population: $\Delta E > a\sqrt{E_{init}}$ only at large wave amplitudes. Using such $\Delta E(E_{init}, B_w, \omega)$ distributions (for all 10^7 trajectories), the probability distribution of $(B_w, \omega/\Omega_{ce})$, and the electron energy spectra at the foreshock for the bow shock events, we plot energy spectra of accelerated electrons. Figures 12b and 12c show that frequencies of whistler waves are usually higher at the bow shock behind the terminator than frequencies of whistler waves at foreshock transient (see Figures 11b and 11c). Although the energy range of electron acceleration by bow shock whistlers is larger than that for bow shock transients (up to 10 keV), bow-shock whistler acceleration is less effective (the ratio of phase space density increase does not exceed 5; it is 10 for foreshock transients).

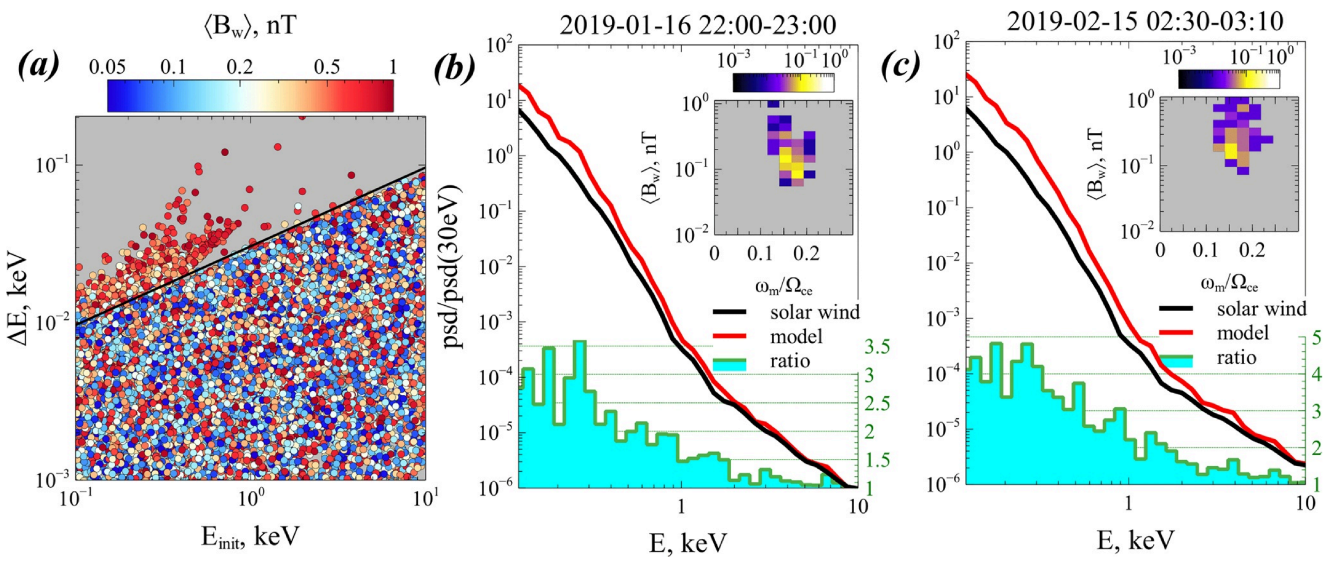

Figure 12. (a) Distribution of 10^4 from 10^7 test particles in the energy, energy gain space. Colors denote wave amplitudes used for each particle orbit. (b and c) Energy spectra of solar wind particles ahead of the foreshock transient (black) and particles accelerated by waves (red) and reflected by a magnetic field gradient for events shown in Figures 3 and 4. The ratio of two spectra is shown to the right vertical axis. Inset panels show probability distributions of observed wave characteristics.

As whistler waves accelerate electrons reflected from magnetic field gradients, these accelerated electrons are expected to mix with the upstream electron population, so there is no simple approach to distinguish whistler wave-accelerated electrons from the background electron population in spacecraft observations. Therefore, the most promising opportunities for verification of the proposed electron acceleration mechanism come from (a) observations of specific wave and field characteristics that allow acceleration up to >10 keV (such energies are not observed in the upstream population) and (b) comparison of multispacecraft observations to resolve the spatial distribution of accelerated electron populations around magnetic field gradients. We leave detailed investigation of such opportunities for future studies. Moreover, investigations of accelerated electron populations should be performed with $\varphi_0 \neq 0$ and v_D determined from detailed analysis of the magnetic gradient configuration.

4. Discussion and Conclusions

In this study, we focused on whistler wave interaction with electrons around magnetic field gradients in the solar wind, such as foreshock transients and the bow shock (for shock crossings behind the terminator). We examined electron acceleration due to a single phase trapping. Reflection of electrons from magnetic field gradients, however, allows reflected electrons to be magnetically trapped between several short, large-amplitude magnetic structures (see, e.g., Schwartz et al., 1992; Wilson et al., 2013); between foreshock transients and the bow shock (see, e.g., T. Z. Liu et al., 2017; T. Z. Liu et al., 2019); or between the magnetopause and shock waves of magnetosheath jets (see, e.g., T. Z. Liu, Hietala, Angelopoulos, Vainio, & Omelchenko, 2020; T. Z. Liu, Hietala, Angelopoulos, Omelchenko, et al., 2020). Such magnetically trapped electrons can experience multiple resonant interactions with whistler waves, resulting in their acceleration to high energies, which are sometimes observed in the foreshock (Wilson et al., 2016) and the shocks of magnetosheath jets (T. Z. Liu, Hietala, Angelopoulos, Vainio, & Omelchenko, 2020). Although these interactions resemble classical electron acceleration in the radiation belts by whistler wave turbulence (Thorne et al., 2013), they may be more effective because of high whistler waves intensity (in comparison with the background field) in the foreshock region. Another potentially important mechanism of electron magnetic trapping (allowing for multiple resonant interaction with whistlers) is supported by large-amplitude compressional low-frequency waves often observed in the foreshock (Lichko & Egedal, 2020; Oka et al., 2019) with whistler wave bursts (Page et al., 2021). Although we modeled nonlinear resonant interactions for relatively weak shock waves, the same model can be applied to the most intense, day-side bow shock where observations of strong whistler waves are reported (Hull et al., 2020; Oka et al., 2019; Page et al., 2021). The wide verity of electromagnetic and plasma waves (e.g., Balikhin et al., 2005; Wilson et al., 2014; Wang et al., 2020, 2021; Perri et al., 2021 and reference therein) on the day-side bow shock, however, requires an additional investigation of trapping stability in the presence of resonant (Nunn, 1986; Shklyar & Zimbardo, 2014) and non-resonant (Artemyev et al., 2015; Brinca, 1978) perturbations.

To conclude, we use THEMIS and ARTEMIS observations of foreshock transients and bow shock behind the terminator to investigate effects of magnetic field gradients on electron resonant interaction with intense whistler waves propagating with frequencies around a fraction of an electron gyrofrequency. We show that the observed waves are sufficiently intense to resonate nonlinearly with electrons, thus providing effective phase trapping. Such resonant trapping for electrons reflected from magnetic field gradients can result in significant acceleration with an energy gain of >100 eV even for a single resonant interaction. The proposed mechanism of electron acceleration may contribute to generation of the energetic electron populations often observed in the foreshock.

Acknowledgments
The work of A. V. Artemyev and I. Vasko was supported by NASA HGI grant 80NSSC21K0581. The authors acknowledge the support of NASA contract NAS5-02099 for use of data from the THEMIS Mission, specifically J. W. Bonnell and F. S. Mozer for use of EFI data, A. Roux and O. LeContel for use of SCM data, and K. H.Glassmeier, U. Auster and W. Baumjohann for the use of FGM data (provided under the lead of the Technical University of Braunschweig and with financial support through the German Ministry for Economy and Technology and the German Center for Aviation and Space (DLR) under contract 50 OC 0302.

Data Availability Statement

Data access (from http://themis.ssl.berkeley.edu) and processing was done using SPEDAS V3.1, see Angelopoulos et al. (2019).

References

Agapitov, O. V., Artemyev, A. V., Mourenas, D., Mozer, F. S., & Krasnoselskikh, V. (2015). Nonlinear local parallel acceleration of electrons through Landau trapping by oblique whistler mode waves in the outer radiation belt. *Geophysical Research Letters*, *42*, 10. https://doi.org/10.1002/2015GL066887

Agapitov, O. V., Mourenas, D., Artemyev, A. V., Mozer, F. S., Hospodarsky, G., Bonnell, J., & Krasnoselskikh, V. (2018). Synthetic empirical chorus wave model from combined van Allen probes and cluster statistics. *Journal of Geophysical Research*, *123*(1), 297–314. https://doi.org/10.1002/2017JA024843

Albert, J. M. (1993). Cyclotron resonance in an inhomogeneous magnetic field. *Physics of Fluids B*, *5*, 2744–2750. https://doi.org/10.1063/1.860715
Albert, J. M., Tao, X., & Bortnik, J. (2013). Aspects of nonlinear wave-particle interactions. In D. Summers, I. U. Mann, D. N. Baker, & M. Schulz (Eds.), *Dynamics of the earth's radiation belts and inner magnetosphere* (pp. 255–264). https://doi.org/10.1029/2012GM001324
Amano, T., Katou, T., Kitamura, N., Oka, M., Matsumoto, Y., Hoshino, M., & Blake, J. B. (2020). Observational evidence for stochastic shock drift acceleration of electrons at the earth's bow shock. *Physical Review Letters*, *124*(6), 065101-1–065101-6. https://doi.org/10.1103/PhysRevLett.124.065101
Angelopoulos, V. (2008). The THEMIS mission. *Space Science Reviews*, *141*, 5–34. https://doi.org/10.1007/s11214-008-9336-1
Angelopoulos, V. (2011). The ARTEMIS mission. *Space Science Reviews*, *165*, 3–25. https://doi.org/10.1007/s11214-010-9687-2
Angelopoulos, V., Cruce, P., Drozdov, A., Grimes, E. W., Hatzigeorgiu, N., King, D. A., & Schroeder, P. (2019). The space physics environment data analysis system (SPEDAS). *Space Science Reviews*, *215*, 9. https://doi.org/10.1007/s11214-018-0576-4
Artemyev, A. V., Agapitov, O., Mourenas, D., Krasnoselskikh, V., Shastun, V., & Mozer, F. (2016). Oblique whistler-mode waves in the earth's inner magnetosphere: Energy distribution, origins, and role in radiation belt dynamics. *Space Science Reviews*, *200*(1–4), 261–355. https://doi.org/10.1007/s11214-016-0252-5
Artemyev, A. V., Krasnoselskikh, V., Agapitov, O., Mourenas, D., & Rolland, G. (2012). Non-diffusive resonant acceleration of electrons in the radiation belts. *Physics of Plasmas*, *19*, 122901. https://doi.org/10.1063/1.4769726
Artemyev, A. V., Mourenas, D., Agapitov, O. V., Vainchtein, D. L., Mozer, F. S., & Krasnoselskikh, V. V. (2015). Stability of relativistic electron trapping by strong whistler or electromagnetic ion cyclotron waves. *Physics of Plasmas*, *22*, 082901-1–082901-12. https://doi.org/10.1063/1.4927774
Artemyev, A. V., Neishtadt, A. I., Vainchtein, D. L., Vasiliev, A. A., Vasko, I. Y., & Zelenyi, L. M. (2018). Trapping (capture) into resonance and scattering on resonance: Summary of results for space plasma systems. *Communications in Nonlinear Science and Numerical Simulations*, *65*, 111–160. https://doi.org/10.1016/j.cnsns.2018.05.004
Artemyev, A. V., Neishtadt, A. I., Vasiliev, A. A., & Mourenas, D. (2016). Kinetic equation for nonlinear resonant wave-particle interaction. *Physics of Plasmas*, *23*(9), 090701-1–090701-4. https://doi.org/10.1063/1.4962526
Artemyev, A. V., Zimbardo, G., Ukhorskiy, A. Y., & Fujimoto, M. (2014). Preferential acceleration of heavy ions in the reconnection outflow region. Drift and surfatron ion acceleration. *Astronomy & Astrophysics*, *562*, A58. https://doi.org/10.1051/0004-6361/201322462
Auster, H. U., Glassmeier, K. H., Magnes, W., Aydogar, O., Baumjohann, W., Constantinescu, D., & Wiedemann, M. (2008). The THEMIS fluxgate magnetometer. *Space Science Reviews*, *141*, 235–264. https://doi.org/10.1007/s11214-008-9365-9
Balikhin, M., Walker, S., Treumann, R., Alleyne, H., Krasnoselskikh, V., Gedalin, M., & Fazakerley, A. (2005). Ion sound wave packets at the quasiperpendicular shock front. *Geophysical Research Letters*, *32*(24), L24106. https://doi.org/10.1029/2005GL024660
Bell, T. F. (1984). The nonlinear gyroresonance interaction between energetic electrons and coherent VLF waves propagating at an arbitrary angle with respect to the earth's magnetic field. *Journal of Geophysical Research*, *89*, 905–918. https://doi.org/10.1029/JA089iA02p00905
Bell, T. F., & Inan, U. S. (1981). Transient nonlinear pitch angle scattering of energetic electrons by coherent VLF wave packets in the magnetosphere. *Journal of Geophysical Research*, *86*, 9047–9063. https://doi.org/10.1029/JA086iA11p09047
Bonnell, J. W., Mozer, F. S., Delory, G. T., Hull, A. J., Ergun, R. E., Cully, C. M., & Harvey, P. R. (2008). The electric field instrument (EFI) for THEMIS. *Space Science Reviews*, *141*, 303–341. https://doi.org/10.1007/s11214-008-9469-2
Brinca, A. L. (1978). Turbulence effects in the cyclotron resonance of monochromatic whistlers. *Geophysical Research Letters*, *5*, 839–842. https://doi.org/10.1029/GL005i010p00839
Burgess, D. (1987). Shock drift acceleration at low energies. *Journal of Geophysical Research*, *92*(A2), 1119–1130. https://doi.org/10.1029/JA092iA02p01119
Cully, C. M., Ergun, R. E., Stevens, K., Nammari, A., & Westfall, J. (2008). The THEMIS digital fields board. *Space Science Reviews*, *141*, 343–355. https://doi.org/10.1007/s11214-008-9417-1
Decker, R. B. (1988). Computer modeling of test particle acceleration at oblique shocks. *Space Science Reviews*, *48*, 195–262. https://doi.org/10.1007/BF00226009
Decker, R. B., & Vlahos, L. (1985). Shock drift acceleration in the presence of waves. *Journal of Geophysical Research*, *90*, 47–56. https://doi.org/10.1029/JA090iA01p00047
Demekhov, A. G., Trakhtengerts, V. Y., Rycroft, M. J., & Nunn, D. (2006). Electron acceleration in the magnetosphere by whistler-mode waves of varying frequency. *Geomagnetism and Aeronomy*, *46*, 711–716. https://doi.org/10.1134/S0016793206060053
Dimmock, A. P., Balikhin, M. A., Krasnoselskikh, V. V., Walker, S. N., Bale, S. D., & Hobara, Y. (2012). A statistical study of the cross-shock electric potential at low Mach number, quasi-perpendicular bow shock crossings using Cluster data. *Journal of Geophysical Research*, *117*, 2210. https://doi.org/10.1029/2011JA017089
Foster, J. C., Erickson, P. J., Baker, D. N., Claudepierre, S. G., Kletzing, C. A., Kurth, W., & Wygant, J. R. (2014). Prompt energization of relativistic and highly relativistic electrons during a substorm interval: Van Allen Probes observations. *Geophysical Research Letters*, *41*, 20–25. https://doi.org/10.1002/2013GL058438
Gan, L., Li, W., Ma, Q., Artemyev, A. V., & Albert, J. M. (2020). Unraveling the formation mechanism for the bursts of electron butterfly distributions: Test particle and quasilinear simulations. *Geophysical Research Letters*, *47*(21), e90749. 1–10. https://doi.org/10.1029/2020GL090749
Gary, S. P., & Feldman, W. C. (1977). Solar wind heat flux regulation by the whistler instability. *Journal of Geophysical Research*, *82*(7), 1087. https://doi.org/10.1029/JA082i007p01087
Gedalin, M. (1996). Ion reflection at the shock front revisited. *Journal of Geophysical Research*, *101*, 4871–4878. https://doi.org/10.1029/95JA03669
Gedalin, M. (1999). Two-stream instability of electrons in the shock front. *Geophysical Research Letters*, *26*(9), 1239–1242. https://doi.org/10.1029/1999GL900239
Gedalin, M. (2020). Large-scale versus small-scale fields in the shock front: Effect on the particle motion. *The Astrophysical Journal*, *895*(1), 59. https://doi.org/10.3847/1538-4357/ab8af0
Goodrich, C. C., & Scudder, J. D. (1984). The adiabatic energy change of plasma electrons and the frame dependence of the cross-shock potential at collisionless magnetosonic shock waves. *Journal of Geophysical Research*, *89*(A8), 6654–6662. https://doi.org/10.1029/JA089iA08p06654
Greenstadt, E. W., Fredricks, R. W., Russell, C. T., Scarf, F. L., Anderson, R. R., & Gurnett, D. A. (1981). Whistler mode wave propagation in the solar wind near the bow shock. *Journal of Geophysical Research: Space Physics*, *86*(A6), 4511–4516. https://doi.org/10.1029/JA086iA06p04511
Horne, R. B. (2007). Plasma astrophysics: Acceleration of killer electrons. *Nature Physics*, *3*, 590–591. https://doi.org/10.1038/nphys703
Hsieh, Y.-K., Kubota, Y., & Omura, Y. (2020). Nonlinear evolution of radiation belt electron fluxes interacting with oblique whistler mode chorus emissions. *Journal of Geophysical Research: Space Physics*, *125*, 1–16. https://doi.org/10.1029/2019ja027465

Hull, A. J., Chaston, C. C., Bonnell, J. W., Damiano, P. A., Wygant, J. R., & Reeves, G. D. (2020). Correlations between dispersive Alfvén wave activity, electron energization, and ion outflow in the inner magnetosphere. *Geophysical Research Letters*, *47*(17), 1–11. https://doi.org/10.1029/2020GL088985

Hull, A. J., Muschietti, L., Oka, M., Larson, D. E., Mozer, F. S., Chaston, C. C., & Hospodarsky, G. B. (2012). Multiscale whistler waves within Earth's perpendicular bow shock. *Journal of Geophysical Research*, *117*, 12104. https://doi.org/10.1029/2012JA017870

Karpman, V. I. (1974). Nonlinear effects in the ELF waves propagating along the magnetic field in the magnetosphere. *Space Science Reviews*, *16*, 361–388. https://doi.org/10.1007/BF00171564

Karpman, V. I., Istomin, J. N., & Shklyar, D. R. (1974). Nonlinear theory of a quasi-monochromatic whistler mode packet in inhomogeneous plasma. *Plasma Physics*, *16*, 685–703. https://doi.org/10.1088/0032-1028/16/8/001

Kennel, C. (1966). Low-frequency whistler mode. *Physics of Fluids*, *9*, 2190–2202. https://doi.org/10.1063/1.1761588

Kennel, C. F. (1969). Consequences of a magnetospheric plasma. *Reviews of Geophysics and Space Physics*, *7*, 379–419. https://doi.org/10.1029/RG007i001p00379

Kennel, C. F., & Engelmann, F. (1966). Velocity space diffusion from weak plasma turbulence in a magnetic field. *Physics of Fluids*, *9*, 2377–2388. https://doi.org/10.1063/1.1761629

Krasnoselskikh, V., Balikhin, M., Walker, S. N., Schwartz, S., Sundkvist, D., Lobzin, V., & Comisel, H. (2013). The dynamic quasiperpendicular shock: Cluster discoveries. *Space Science Reviews*, *178*, 535–598. https://doi.org/10.1007/s11214-013-9972-y

Kuramitsu, Y., & Krasnoselskikh, V. (2005a). Gyroresonant surfing acceleration. *Physical Review Letters*, *94*(3), 031102-1–031102-4. https://doi.org/10.1103/PhysRevLett.94.031102

Kuramitsu, Y., & Krasnoselskikh, V. (2005b). Particle acceleration by elliptically and linearly polarized waves in the vicinity of quasi-parallel shocks. *Journal of Geophysical Research*, *110*, 10108. https://doi.org/10.1029/2005JA011048

Le Contel, O., Roux, A., Jacquey, C., Robert, P., Berthomier, M., Chust, T., & Singer, H. (2009). Quasi-parallel whistler mode waves observed by THEMIS during near-earth dipolarizations. *Annales Geophysicae*, *27*, 2259–2275. https://doi.org/10.5194/angeo-27-2259-2009

Le Contel, O., Roux, A., Robert, P., Coillot, C., Bouabdellah, A., deLa Porte, B., & Larson, D. (2008). First results of the THEMIS search coil magnetometers. *Space Science Reviews*, *141*, 509–534. https://doi.org/10.1007/s11214-008-9371-y

Lefebvre, B., Schwartz, S. J., Fazakerley, A. F., & Décréau, P. (2007). Electron dynamics and cross-shock potential at the quasi-perpendicular Earth's bow shock. *Journal of Geophysical Research*, *112*, 9212. https://doi.org/10.1029/2007JA012277

Leroy, M. M., & Mangeney, A. (1984). A theory of energization of solar wind electrons by the earth's bow shock. *Annales Geophysicae*, *2*, 449–456.

Lever, E. L., Quest, K. B., & Shapiro, V. D. (2001). Shock surfing vs. shock drift acceleration. *Geophysical Research Letters*, *28*, 1367–1370. https://doi.org/10.1029/2000GL012516

Li, W., & Hudson, M. K. (2019). Earth's van Allen radiation belts: From discovery to the van Allen probes era. *Journal of Geophysical Research*, *124*(11), 8319–8351. https://doi.org/10.1029/2018JA025940

Li, W., Thorne, R. M., Bortnik, J., Baker, D. N., Reeves, G. D., Kanekal, S. G., & Green, J. C. (2015). Solar wind conditions leading to efficient radiation belt electron acceleration: A superposed epoch analysis. *Geophysical Research Letters*, *42*, 6906–6915. https://doi.org/10.1002/2015GL065342

Lichko, E., & Egedal, J. (2020). Magnetic pumping model for energizing superthermal particles applied to observations of the Earth's bow shock. *Nature Communications*, *11*, 2942. https://doi.org/10.1038/s41467-020-16660-4

Liu, T. Z., Angelopoulos, V., & Lu, S. (2019). Relativistic electrons generated at Earth's quasi-parallel bow shock. *Science Advances*, *5*(7), 1–5. https://doi.org/10.1126/sciadv.aaw1368

Liu, T. Z., Hietala, H., Angelopoulos, V., Omelchenko, Y., Vainio, R., & Plaschke, F. (2020). Statistical study of magnetosheath jet-driven bow waves. *Journal of Geophysical Research*, *125*(7), e2019JA027710. https://doi.org/10.1029/2019JA027710

Liu, T. Z., Hietala, H., Angelopoulos, V., Vainio, R., & Omelchenko, Y. (2020). Electron acceleration by magnetosheath jet-driven bow waves. *Journal of Geophysical Research*, *125*(7), e2019JA027709. https://doi.org/10.1029/2019JA027709

Liu, T. Z., Lu, S., Angelopoulos, V., Hietala, H., & Wilson, L. B. (2017). Fermi acceleration of electrons inside foreshock transient cores. *Journal of Geophysical Research*, *122*(9), 9248–9263. https://doi.org/10.1002/2017JA024480

Liu, T. Z., Turner, D. L., Angelopoulos, V., & Omidi, N. (2016). Multipoint observations of the structure and evolution of foreshock bubbles and their relation to hot flow anomalies. *Journal of Geophysical Research*, *121*(6), 5489–5509. https://doi.org/10.1002/2016JA022461

Liu, Z., Turner, D. L., Angelopoulos, V., & Omidi, N. (2015). THEMIS observations of tangential discontinuity-driven foreshock bubbles. *Geophysical Research Letters*, *42*(19), 7860–7866. https://doi.org/10.1002/2015GL065842

Lyons, L. R., Thorne, R. M., & Kennel, C. F. (1972). Pitch-angle diffusion of radiation belt electrons within the plasmasphere. *Journal of Geophysical Research*, *77*, 3455–3474. https://doi.org/10.1029/JA077i019p03455

McFadden, J. P., Carlson, C. W., Larson, D., Ludlam, M., Abiad, R., Elliott, B., & Angelopoulos, V. (2008). The THEMIS ESA plasma instrument and in-flight calibration. *Space Science Reviews*, *141*, 277–302. https://doi.org/10.1007/s11214-008-9440-2

Mozer, F. S., & Sundkvist, D. (2013). Electron demagnetization and heating in quasi-perpendicular shocks. *Journal of Geophysical Research*, *118*(9), 5415–5420. https://doi.org/10.1002/jgra.50534

Muschietti, L., & Lembège, B. (2017). Two-stream instabilities from the lower-hybrid frequency to the electron cyclotron frequency: Application to the front of quasi-perpendicular shocks. *Annales Geophysicae*, *35*(5), 1093–1112. https://doi.org/10.5194/angeo-35-1093-2017

Ni, B., Thorne, R. M., Zhang, X., Bortnik, J., Pu, Z., Xie, L., & Gu, X. (2016). Origins of the earth's diffuse auroral precipitation. *Space Science Reviews*, *200*, 205–259. https://doi.org/10.1007/s11214-016-0234-7

Nunn, D. (1971). Wave-particle interactions in electrostatic waves in an inhomogeneous medium. *Journal of Plasma Physics*, *6*, 291. https://doi.org/10.1017/S0022377800006061

Nunn, D. (1986). A nonlinear theory of sideband stability in ducted whistler mode waves. *Planatary Space Science*, *34*, 429–451. https://doi.org/10.1016/0032-0633(86)90032-2

Oka, M., Otsuka, F., Matsukiyo, S., Wilson, I.L. B., Argall, M. R., et al. (2019). Electron scattering by low-frequency whistler waves at earth's bow shock. *The Astrophysical Journal*, *886*(1), 53. https://doi.org/10.3847/1538-4357/ab4a81

Oka, M., Wilson, L. B., III, Phan, T. D., Hull, A. J., Amano, T., Hoshino, M., & Lindqvist, P. A. (2017). Electron scattering by high-frequency whistler waves at earth's bow shock. *The Astrophysical Journal Letters*, *842*, L11. https://doi.org/10.3847/2041-8213/aa7759

Omidi, N., Eastwood, J. P., & Sibeck, D. G. (2010). Foreshock bubbles and their global magnetospheric impacts. *Journal of Geophysical Research*, *115*(A6), A06204. https://doi.org/10.1029/2009JA014828

Omura, Y., Furuya, N., & Summers, D. (2007). Relativistic turning acceleration of resonant electrons by coherent whistler mode waves in a dipole magnetic field. *Journal of Geophysical Research*, *112*, 6236. https://doi.org/10.1029/2006JA012243

Omura, Y., Katoh, Y., & Summers, D. (2008). Theory and simulation of the generation of whistler-mode chorus. *Journal of Geophysical Research*, *113*, 4223. https://doi.org/10.1029/2007JA012622

Omura, Y., Matsumoto, H., Nunn, D., & Rycroft, M. J. (1991). A review of observational, theoretical and numerical studies of VLF triggered emissions. *Journal of Atmospheric and Terrestrial Physics*, *53*, 351–368. https://doi.org/10.1016/0021-9169(91)90031-2

Page, B., Vasko, I. Y., Artemyev, A. V., & Bale, S. D. (2021). Generation of high-frequency whistler waves in the earth's quasi-perpendicular bow shock. *The Astrophysical Journal Letters*, *919*(2), L17. https://doi.org/10.3847/2041-8213/ac2748

Perri, S., Perrone, D., Roberts, O., Settino, A., Yordanova, E., Sorriso-Valvo, L., & Valentini, F. (2021). Nature of electrostatic fluctuations in the terrestrial magnetosheath. *The Astrophysical Journal*, *919*(2), 75. https://doi.org/10.3847/1538-4357/ac13a2

Sagdeev, R. Z., & Shafranov, V. D. (1961). On the instability of a plasma with an anisotropic distribution of velocities in a magnetic field. *Soviet Physics JETP*, *12*(1), 130–132.

Sauer, K., Baumgaerte, K., & Sydora, R. D. (2020). Gap formation around $\omega_e/2$ and generation of low-band whistler waves by landau-resonant electrons in the magnetosphere: Predictions from dispersion theory. *Earth and Planetary Physics*, *4*, 138. https://doi.org/10.26464/epp2020020

Sazhin, S. (1993). *Whistler-mode waves in a hot plasma*. Cambridge University Press.

Schwartz, S. J., Burgess, D., Wilkinson, W. P., Kessel, R. L., Dunlop, M., & Luehr, H. (1992). Observations of short large-amplitude magnetic structures at a quasi-parallel shock. *Journal of Geophysical Research*, *97*(A4), 4209–4227. https://doi.org/10.1029/91JA02581

Schwartz, S. J., Ergun, R., Kucharek, H., Wilson, L., Chen, L.-J., Goodrich, K., & Strangeway, R. (2021). Evaluating the deHoffmann-Teller cross-shock potential at real collisionless shocks. *Journal of Geophysical Research*, *126*(8), e2021JA029295. https://doi.org/10.1029/2021JA029295

Schwartz, S. J., Henley, E., Mitchell, J., & Krasnoselskikh, V. (2011). Electron temperature gradient scale at collisionless shocks. *Physical Review Letters*, *107*(21), 215002. https://doi.org/10.1103/PhysRevLett.107.215002

Scudder, J. D. (1995). A review of the physics of electron heating at collisionless shocks. *Advances in Space Research*, *15*, 181–223. https://doi.org/10.1016/0273-1177(94)00101-6

Shi, X., Liu, T. Z., Angelopoulos, V., & Zhang, X.-J. (2020). Whistler mode waves in the compressional boundary of foreshock transients. *Journal of Geophysical Research*, *125*(8), e2019JA027758. https://doi.org/10.1029/2019JA027758

Shklyar, D. R. (1981). Stochastic motion of relativistic particles in the field of a monochromatic wave. *Soviet Physics Journal of Experimental and Theoretical Physics*, *53*, 1197–1192.

Shklyar, D. R. (2011). On the nature of particle energization via resonant wave-particle interaction in the inhomogeneous magnetospheric plasma. *Annales Geophysicae*, *29*, 1179–1188. https://doi.org/10.5194/angeo-29-1179-2011

Shklyar, D. R. (2017). Energy transfer from lower energy to higher-energy electrons mediated by whistler waves in the radiation belts. *Journal of Geophysical Research*, *122*(1), 640–655. https://doi.org/10.1002/2016JA02326310.1002/2016JA023263

Shklyar, D. R., & Matsumoto, H. (2009). Oblique whistler-mode waves in the inhomogeneous magnetospheric plasma: Resonant interactions with energetic charged particles. *Surveys in Geophysics*, *30*, 55–104. https://doi.org/10.1007/s10712-009-9061-7

Shklyar, D. R., & Zimbardo, G. (2014). Particle dynamics in the field of two waves in a magnetoplasma. *Plasma Physics and Controlled Fusion*, *56*(9), 1–12. https://doi.org/10.1088/0741-3335/56/9/095002

Solovev, V. V., & Shkliar, D. R. (1986). Particle heating by a low-amplitude wave in an inhomogeneous magnetoplasma. *Soviet Physics Journal of Experimental and Theoretical Physics*, *63*, 272–277.

Stix, T. H. (1962). *The theory of plasma waves*.

Tao, X., Thorne, R. M., Li, W., Ni, B., Meredith, N. P., & Horne, R. B. (2011). Evolution of electron pitch angle distributions following injection from the plasma sheet. *Journal of Geophysical Research*, *116*, A04229. https://doi.org/10.1029/2010JA016245

Thorne, R. M., Li, W., Ni, B., Ma, Q., Bortnik, J., Chen, L., & Kanekal, S. G. (2013). Rapid local acceleration of relativistic radiation-belt electrons by magnetospheric chorus. *Nature*, *504*, 411–414. https://doi.org/10.1038/nature12889

Thorne, R. M., Ni, B., Tao, X., Horne, R. B., & Meredith, N. P. (2010). Scattering by chorus waves as the dominant cause of diffuse auroral precipitation. *Nature*, *467*, 943–946. https://doi.org/10.1038/nature09467

Tokar, R. L., Gurnett, D. A., & Feldman, W. C. (1984). Whistler mode turbulence generated by electron beams in earth's bow shock. *Journal of Geophysical Research*, *89*(A1), 105–114. https://doi.org/10.1029/JA089iA01p00105

Tong, Y., Vasko, I. Y., Pulupa, M., Mozer, F. S., Bale, S. D., Artemyev, A. V., & Krasnoselskikh, V. (2019). Whistler wave generation by Halo electrons in the solar wind. *The Astrophysical Journal Letters*, *870*(1), L6. https://doi.org/10.3847/2041-8213/aaf734

Trakhtengerts, V. Y. (1966). Stationary states of the Earth's outer radiation zone. *Geomagnetism and Aeronomy*, *6*, 827–836.

Turner, D. L., Omidi, N., Sibeck, D. G., & Angelopoulos, V. (2013). First observations of foreshock bubbles upstream of Earth's bow shock: Characteristics and comparisons to HFAs. *Journal of Geophysical Research*, *118*(4), 1552–1570. https://doi.org/10.1002/jgra.50198

Ucer, D., & Shapiro, V. D. (2001). Unlimited relativistic shock surfing acceleration. *Physical Review Letters*, *87*(7), 075001-1–075001-4. https://doi.org/10.1103/PhysRevLett.87.075001

Vainchtein, D., Zhang, X.-J., Artemyev, A., Mourenas, D., Angelopoulos, V., & Thorne, R. M. (2018). Evolution of electron distribution driven by nonlinear resonances with intense field-aligned chorus waves. *Journal of Geophysical Research*, *123*, 8149–8169. https://doi.org/10.1029/2018ja025654

Vasko, I. Y., Kuzichev, I. V., Artemyev, A. V., Bale, S. D., Bonnell, J. W., & Mozer, F. S. (2020). On quasi-parallel whistler waves in the solar wind. *Physics of Plasmas*, *27*(8), 082902-1–082902-13. https://doi.org/10.1063/5.0003401

Vedenov, A. A., Velikhov, E., & Sagdeev, R. (1962). Quasilinear theory of plasma oscillations. *Nuclear Fusion* (2), 465–475.

Veltri, P., & Zimbardo, G. (1993a). Electron-whistler interaction at the earth's bow shock: 1. Whistler instability. *Journal of Geophysical Research*, *98*(A8), 13325–13334. https://doi.org/10.1029/93JA00812

Veltri, P., & Zimbardo, G. (1993b). Electron-whistler interaction at the earth's bow shock: 2. Electron pitch angle diffusion. *Journal of Geophysical Research*, *98*, 13335–13346. https://doi.org/10.1029/93JA01144

Walker, S., Alleyne, H., Balikhin, M., André, M., & Horbury, T. (2004). Electric field scales at quasi-perpendicular shocks. *Annales Geophysicae*, *22*, 2291–2300. https://doi.org/10.5194/angeo-22-2291-2004

Wang, R., Vasko, I. Y., Mozer, F. S., Bale, S. D., Artemyev, A. V., Bonnell, J. W., & Strangeway, R. (2020). Electrostatic turbulence and Debye-scale structures in collisionless shocks. *The Astrophysical Journal Letters*, *889*(1), L9. https://doi.org/10.3847/2041-8213/ab6582

Wang, R., Vasko, I. Y., Mozer, F. S., Bale, S. D., Kuzichev, I. V., Artemyev, A. V., & Strangeway, R. (2021). Electrostatic solitary waves in the earth's bow shock: Nature, properties, lifetimes, and origin. *Journal of Geophysical Research*, *126*(7), e2021JA029357. https://doi.org/10.1029/2021JA029357

Wilson, L. B. (2016). *Low Frequency Waves at and Upstream of Collisionless Shocks* (Vol. 216, pp. 269–291). Washington DC American Geophysical Union Geophysical Monograph Series. https://doi.org/10.1002/9781119055006.ch16

Wilson, L. B., Koval, A., Sibeck, D. G., Szabo, A., Cattell, C. A., Kasper, J. C., & Wilber, M. (2013). Shocklets, SLAMS, and field-aligned ion beams in the terrestrial foreshock. *Journal of Geophysical Research*, *118*, 957–966. https://doi.org/10.1029/2012JA018186

Wilson, L. B., Sibeck, D. G., Breneman, A. W., Contel, O. L., Cully, C., Turner, D. L., & Malaspina, D. M. (2014). Quantified energy dissipation rates in the terrestrial bow shock: 2. Waves and dissipation. *Journal of Geophysical Research*, *119*, 6475–6495. https://doi.org/10.1002/2014JA019930

Wilson, L. B., Sibeck, D. G., Turner, D. L., Osmane, A., Caprioli, D., & Angelopoulos, V. (2016). Relativistic electrons produced by foreshock disturbances observed upstream of earth's bow shock. *Physical Review Letters*, *117*(21), 215101. https://doi.org/10.1103/PhysRevLett.117.215101

Wu, C. S. (1984). A fast Fermi process: Energetic electrons accelerated by a nearly perpendicular bow shock. *Journal of Geophysical Research*, *89*(A10), 8857–8862. https://doi.org/10.1029/JA089iA10p08857

Zhang, X., Angelopoulos, V., Artemyev, A. V., & Liu, J. (2018). Whistler and electron firehose instability control of electron distributions in and around dipolarizing flux bundles. *Geophysical Research Letters*, *45*, 9380–9389. https://doi.org/10.1029/2018GL079613

Zhang, X. J., Mourenas, D., Artemyev, A. V., Angelopoulos, V., Bortnik, J., Thorne, R. M., & Hospodarsky, G. B. (2019). Nonlinear electron interaction with intense chorus waves: Statistics of occurrence rates. *Geophysical Research Letters*, *46*(13), 7182–7190. https://doi.org/10.1029/2019GL083833

Zhang, X. J., Thorne, R., Artemyev, A., Mourenas, D., Angelopoulos, V., Bortnik, J., & Hospodarsky, G. B. (2018). Properties of intense field-aligned lower-band chorus waves: Implications for nonlinear wave-particle interactions. *Journal of Geophysical Research*, *123*(7), 5379–5393. https://doi.org/10.1029/2018JA025390

Zhang, Y., Matsumoto, H., Kojima, H., & Omura, Y. (1999). Extremely intense whistler mode waves near the bow shock: Geotail observations. *Journal of Geophysical Research*, *104*, 449–462. https://doi.org/10.1029/1998JA900049